PHOTOACOUSTIC LIFETIME IMAGING AND ITS BIOMEDICAL APPLICATIONS

A DISSERTATION
SUBMITTED TO THE FACULTY OF
UNIVERSITY OF MINNESOTA
BY

Qi Shao

IN PARTIAL FULFILLMENT OF THE REQUIREMENTS
FOR THE DEGREE OF
DOCTOR OF PHILOSOPHY

Shai Ashkenazi, Adviser

January 2016

© Qi Shao 2016

Acknowledgements

This work would not have been possible without the support (both professional and personal) of a great number of people. First, I would like to thank my advisor, Professor Shai Ashkenazi, for his guidance throughout this endeavor. I waded into the Ph.D. program because I wanted to be sure that I could find a project I cared about and an advisor that I respected and could learn from. I think I developed a lot during my time here in the Photoacoustic and Ultrasound Lab, thanks in a large part to our candid discussions. Besides being an outstanding advisor, I am deeply inspired by his approachable personality, and his attitude towards work with devotion, optimism, and pragmatism.

Secondly, I would like to thank my committee members, past and present, for their time in reviewing my work. They include Dr. Taner Akkin, Dr. John Bischof and Dr. Bin He.

One of the greatest opportunities and challenges of my project was the collaborative nature of this research. I am also very fortunate to work in a friendly and supportive team in the Photoacoustic and Ultrasound Lab, with lab members Clay Sheaff, Mohammad Amin Tadayon, Ekaterina Morgounova and Supriya Thathachary. I would like to express my gratitude from people in Dr. Bischof's group for the part of study described in this dissertation, especially Chunlan Jiang, Jeunghwan Choi. I would also thank Dr. Merrill A. Biel for his expertise and professional guidance.

Besides the research giving in details in this dissertation, I am grateful to work part time in Bioheat and Mass Transfer Lab and IEM Cancer Animal Core lab, where I have been exposed to a variety of fascinating research across the campus. These people and work expand greatly my horizon and deepen my understanding in lots of disciplines. I cherish all opportunities working together. They are Navid Manuchehrabadi, Connie Chung, Michael Etheridge and Feng Liu in Dr. John Bischof's lab; Jiaen Liu, Kai Yu, Xiaotong Zhang, Yicun Wang and Leo Mariappan in Dr. Bin He's lab; Katie Hurley, Zhe Gao and Hattie Ring in Dr. Christy Haynes's lab; Jinjin Zhang in Dr. Michael Garwood's lab; Santosh Kondeti from Dr. Peter Bruggeman's lab;

My work cannot be made possible without the financial support from Department of Biomedical Engineering, doctoral dissertation fellowship from the Graduate School. Other financial supports (in part) are from NIH R21 EB016763, R21 CA135027, R01 CA183749, IEM Cancer Animal Core Lab, Boston Scientific, Galil Medical.

Last, but certainly not least, I would like to thank my family and friends for helping me making through challenges and keeping my spirits high while doing my Ph.D. work. And finally, thanks to my incredibly understanding girlfriend, Yu Yu, for keeping my life exciting. I love research (everyone around me knows it for sure), however, I love her more than I care about my work.

Dedication

I would like to dedicate this thesis to my incredible parents, Hui Shao and Wei Huang. Their hard work, endless support and encouragement, and caring for everyone around them, has set an amazing example to live by and I hope that they realize it is reflected in their child and family.

Table of Contents

List of Figures

Preface

While the core of this work is composed of 5 stand-alone chapters, together they provide a cohesive story which maps out the development and application of photoacoustic lifetime technology. Without exception, contents of all chapters have been scrutinized, either through committee members of established professors (chapter 1 and 4) or peer-review process by prestigious journals (chapter 2, 3 and 5). Even though this approach of organizing this dissertation introduces some inconsistencies in flow of ideas, but it ensures that the contents of this dissertation has been fully vetted by the scientific community and is up to the highest level of writing standards.

Chapter 1 outlines the science behind the photoacoustic lifetime imaging and its engineering approach of the imaging system towards in vivo application. The chapter focus on the development of imaging methods from basic ideas in physical chemistry to actual measurements by photoacoustic method. Implementation of multiple optimizations inspired by the booming field of photoacoustic imaging was then introduced. This chapter consists of the author's thesis proposal in doctoral written preliminary exam (WPE) and the statement for applying doctoral dissertation fellowship (DDF). The contents have been updated to reflect the comments and suggestions made by reviewers from both committee.

Chapter 2 describes a new approach based on in vivo application of photoacoustic lifetime imaging (PALI) to map the distribution of oxygen partial pressure (pO_2) in tissue. A multimodal imaging system was designed and built to achieve ultrasound (US), photoacoustic, and PALI imaging within the same system. Nude mice bearing LNCaP xenograft hindlimb tumors were used as the target tissue. Hypoxic regions were identified within the tumor in a combined US/PALI image. Finally, the statistical distributions of pO_2 in tumor, normal, and control tissues were compared with measurements by a needle-mounted oxygen probe. A statistically significant drop in mean pO_2 was consistently detected by both methods in tumors.

Chapter 3 reports a direct and noninvasive in vivo imaging modality based on the photoacoustic lifetime which overcomes certain drawbacks of the existing methods. Two studies are presented which photoacoustic lifetime imaging (PALI) was applied to monitor changes of tissue oxygen induced by external modulations. In first study, PALI is demonstrated to be able to reflect the change in oxygen level with respect to normal, oxygen-rich, and oxygen-poor breathing conditions. In the second study, the drop of tissue pO_2 resulted from acute ischemia and recovery from hypoxia by reperfusion were tracked and observed by PALI.

Chapter 4 presents the work on developing a treatment/imaging modality (PDT-PALI) that integrates PDT and a combined ultrasound/photoacoustic imaging system. The system provides real-time feedback of three essential parameters namely: tissue oxygen, light penetration in tumor location, and distribution of photosensitizer. Tissue oxygen imaging is performed by applying PALI, which relies on photoacoustic probing of oxygen-dependent, excitation lifetime of Methylene Blue (MB) photosensitizer. Lifetime information can also be used to generate image showing the distribution of photosensitizer. The level and penetration depth of PDT illumination can be deduced from photoacoustic imaging at the same wavelength. All images will be combined with ultrasound B-mode images for anatomical reference. The ideas and approaches were developed before and during the preparation for the proposal of NIH R01CA183749 (optimizing cancer photodynamic therapy using photoacoustic lifetime imaging).

Chapter 5 presents the results demonstrating the ability of photoacoustic imaging to probe the lifetime contrast between monomers and dimers with high sensitivity in cylindrical phantoms. These results suggest that photoacoustic imaging can be used to selectively detect the presence of monomers. This chapter also report the synthesis and testing of a matrix metalloproteinase 2 (MMP-2) specific peptide probe capable of changing its transient photoacoustic lifetime from short to long after activation. It is demonstrated that using a pump-probe photoacoustic imaging approach that the cleaved probe exhibits a transient signal with lifetime comparable to that of MB monomers, whereas no lifetime was detected for the intact probe.

Chapter 1 Development of lifetime imaging by photoacoustic pump-probe approach

1.1 Fluorophore excited state lifetime and its application to oxygen sensing

The lifetime of fluorophore's excited state is typically an intrinsic property of the fluorophore, determined by the quantum transition amplitude between the initial and final states. In many cases, interactions with the environment can shorten the unperturbed lifetime. This mechanism forms the basis for a wide range of fluorescent sensors applied to biological systems. [1]

A typical example of fluorophore's excited state lifetime sensing is oxygen sensitive dyes.[2, 3]. These dyes can be excited into a triplet state, which has a relatively long lifetime due to the "forbidden" (spin-flip) nature of the relaxation to the ground state. However, intermolecular collisions with oxygen (in its triplet ground state) can quench the excited state. Measuring the excited state lifetime provides a quantitative measure of oxygen concentration in the environment. This enables tissue oxygenation imaging as shown in Fig. 1. Mapping this lifetime in tissue enables tissue oxygenation imaging.[4]

In most applications, the lifetime is evaluated by measuring the decay of the fluorescent signal. The lifetime of decaying fluorescent signal is computed by fitting the fluorescent intensity as a function of the time after excitation. Compared to fluorescent intensity measurements, lifetime measurements are much more robust and stable due to the fact that measured insensitivity can be affected by dye concentration, excitation intensity, and light absorption in tissue. Therefor the lifetime obtained relies solely on the interaction of the fluorophore with its environment.

Among the oxygen-sensitive dyes, the unique properties of Methylene Blue (MB) make it suitable for biomedical applications. MB has a strong absorption peak at 660 nm (extinction coefficient is 72,000 cm^{-1} /M). At this wavelength, tissue optical absorption is relatively low, allowing imaging at a larger penetration depth. MB is a water-soluble dye that is widely used in clinical diagnostic and therapeutic applications [5-7], due to due to its low cytotoxicity and efficient clearance from the body [8, 9]. MB also has a high efficiency (quantum yield of 0.52) of being into oxygen-sensitive triplet state after being excited. Excited MB exhibits substantial differential in the length of lifetime on oxygen concentration, with 79.5 μs in degassed water (pO_2=0) and 1.8 μs in air-saturated aqueous solution (pO_2=150 mmHg) [10].

The oxygen dependent lifetime is described by Stern–Volmer relationship.

$$T^0 / T = 1 + k_Q T^0 p\mathrm{O}_2 ,$$

where T^0 and T are the triplet lifetimes at zero oxygen and at a given pO_2 (in mmHg) respectively. k_Q is a constant with unit $mmHg^{-1}s^{-1}$, and it's related to the frequency of collisions of MB molecule in its excited-state with molecular oxygen.

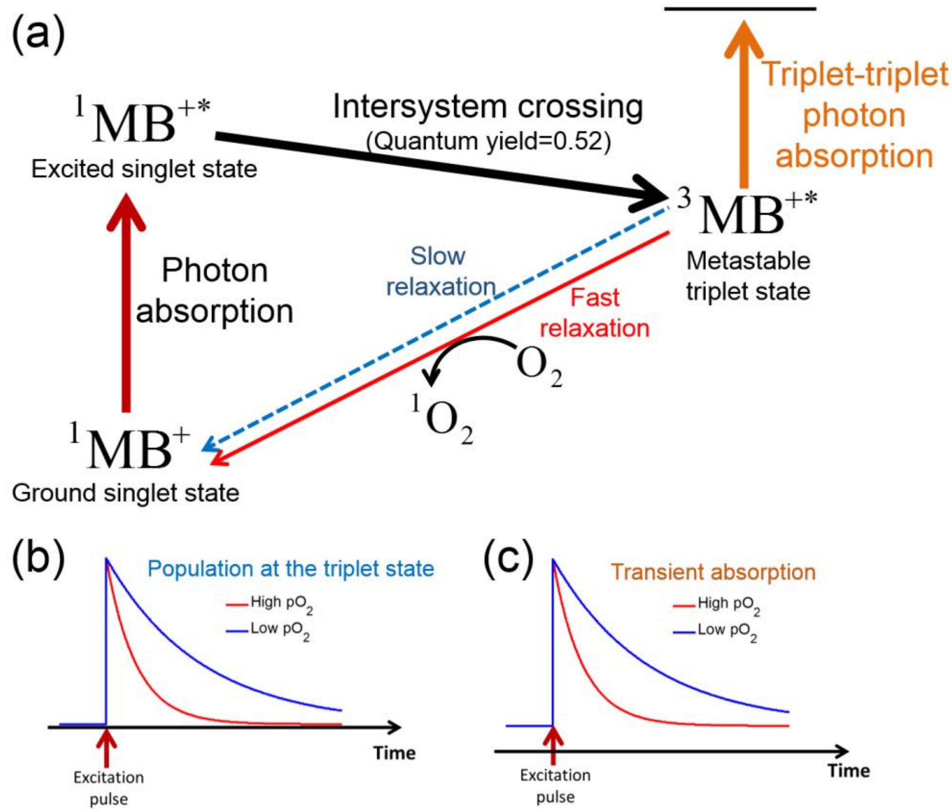

Figure 1 The photo-physics of an oxygen-sensitive dye. (a) Methylene Blue (MB) is given as an example of oxygen-sensitive dye. $^{1}MB^{+}$, $^{1}MB^{+*}$, and $^{3}MB^{+*}$ are methylene blue ground state, singlet and triplet excited states, respectively. The pump laser (red arrow) excites MB molecules at ground singlet state into the singlet state by photon absorption. A large portion (quantum yield of 0.52) of excited singlet state molecules cross to triplet state by intersystem crossing. MB at triplet state absorbs the probe laser (orange arrow) and generates photoacoustic signal. MB at triplet state decays to ground state via either slow non-radiative (blue dash arrow) decay or oxygen quenching (red solid arrow). The relative positions of the species presented in this scheme do not represent their actual energy level. (b) The change of the population at the excited triplet state with respect to time. The population at excited state peaks immediately (within a few nanosecond) after the excitation pulse. The decrease of this population (microsecond to millisecond) is dependent on oxygen concentration (oxygen partial pressure, pO_2). The more oxygen the dye interacts with, the faster the decay is. (c) The oxygen-dependent transient absorption with respect to time. Following excitation, the population at excited state deceases, the absorption by triplet-triplet absorption also decrease proportionally. Combined with background absorption (by tissue), the absorption of light matching triplet-triplet absorption is also oxygen-dependent.

1.2 Photoacoustic pump-probe approach for measuring lifetime

One of the major difficulties in applying fluorescent methods for clinical oxygen imaging is the loss of spatial information due to strong light scattering. Pure optical imaging methodologies suffer from significantly degraded spatial resolution with depth due to optical scattering in soft tissues. Phosphorescence imaging cannot resolve depth and therefore is not applicable to tissue imaging.

Photoacoustic imaging (PAI) is an imaging modality based on generation of acoustic waves by the absorption of light. [11] PAI combines ultrasonic resolution with high contrast of light absorption. Ultrasound imaging can reach a higher depth in biological tissue than pure optical imaging. PAI provides high optical contrast in large volumes of biological tissues at the resolution of ultrasound imaging. The resolution of PAI is determined by the ultrasound used for photoacoustic (PA) signal detection and therefore resembles that of ultrasound imaging. Imaging depth of PAI depends on diffused light penetrating tissue and can reach up to a few cm.

Photoacoustic lifetime is a photoacoustic technique for probing the lifetime of fluorophore's excited state. In this method as shown in Fig. 2, the first laser pulse (pump) drives the dye into the excited state, at which it exhibits a transient absorption. The transience can be probed by a second laser (probe) to generate photoacoustic wave, and the photoacoustic imaging reflecting the relative population of the excited and ground states can be obtained. By changing the time delay between the pulses (pump-probe), the decay of the excited state population can be monitored and the excited state lifetime can be extracted.

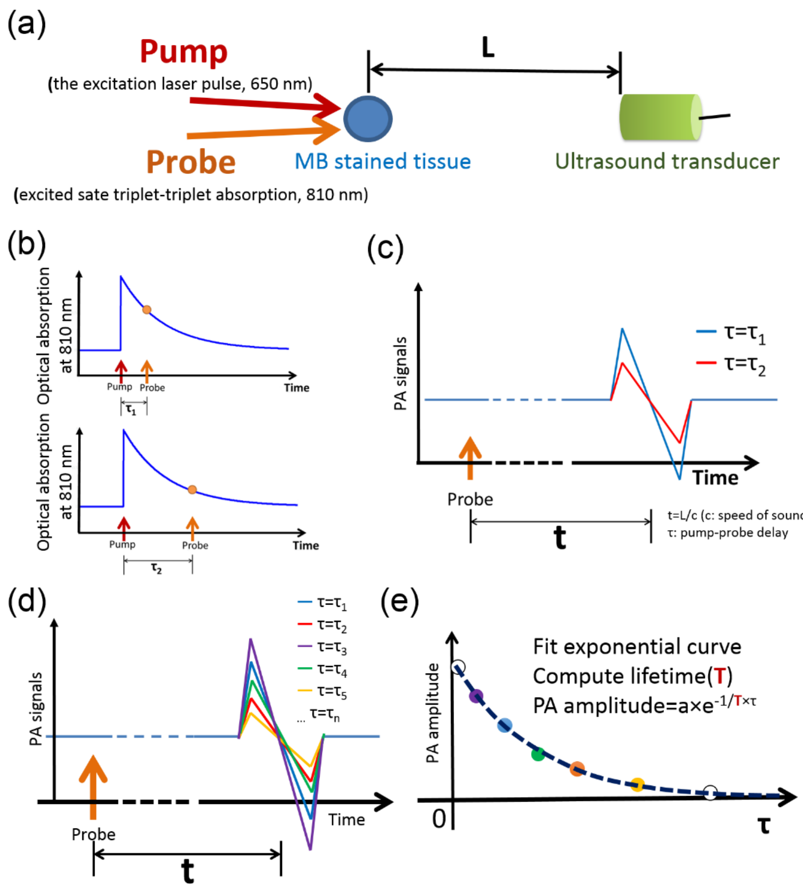

Figure 2 Photoacoustic pump-probe approach for sensing oxygen. (a) The measurement of an object (MB stained tissue as an example) requires two lasers pulses (pump and probe) and an ultrasound transducer with a distance L from the object. The pump is defined as the excitation laser, and the probe is for probing the triplet-triplet absorption. (b) Pump-probe delay of τ_1 and τ_2 are applied to capture the optical time-dependent absorption. (c) Due to the transient absorption, the photoacoustic (PA) signal relies on the pump-probe delay. The location of the object is determined by the speed of sound and the time between probe laser and the PA signal that changes with τ. (d) By applying a series of pump-probe delays, different PA signal amplitudes are achieved. (e) The PA amplitudes are fit with an exponential function to the pump-probe delay, and the lifetime is computed.

To verify the basic principle of oxygen sensing by PA method, we applied the system to a single object. The object is a single plastic tube with MB inside, the transducer is placed about 3 cm from the tube. The oxygen content is controlled by the amount of Nitrogen bubbled into the MB solution within a cell. A pump keeps the circulation system flowing with constant rate to and from the gas mixture cell, as shown in Fig. 3.

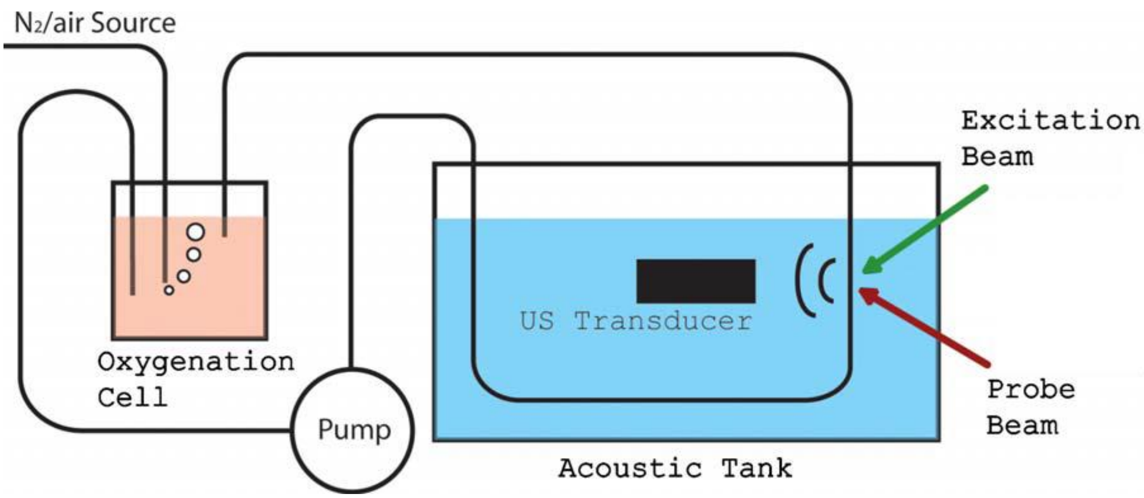

Figure 3 Experimental setup of photoacoustic pump-probe lifetime measurement of oxygen. The setup includes a closed flow circulating oxygen-sensitive dye, in plastic tubing, a peristaltic pump, and an oxygenation cell, adapted from [12]. The excitation and probe beams illuminate a section of the tubing. Photoacoustic signals are detected by an ultrasound transducer. Water tank is used for ultrasound coupling between the tubing and the transducer.

The raw PA signal is recorded at a set of time delays. An example of the PA amplitude change with time delay of probe and pump is shown in Fig. 4(a). To extract the transient absorption of MB and compute the lifetime, the photoacoustic amplitude is fit exponentially with the pump-probe delays. The PA amplitude is direct proportional to the absorption, and the lifetime of transient absorption depends on the pO_2. Fig. 4(b) gives an example of the extracted transient absorption of MB under two distinct oxygen levels.

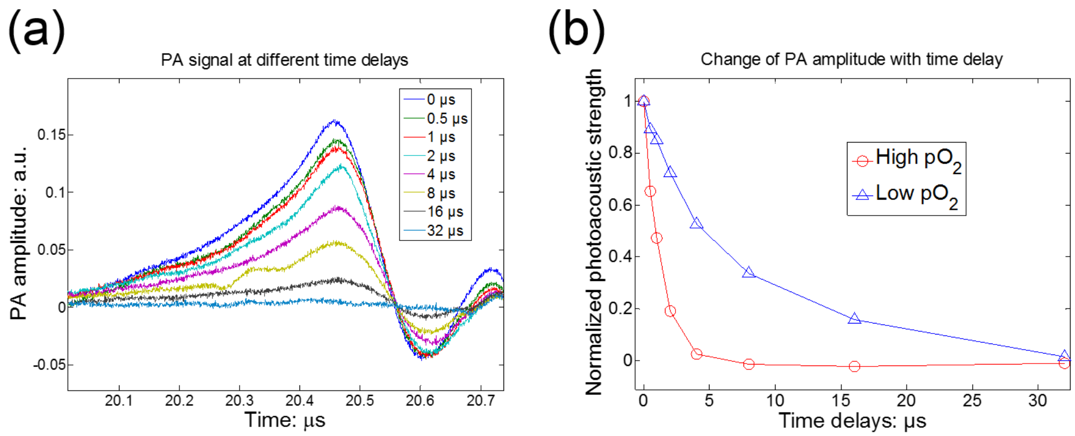

Figure 4 Photoacoustic signal changes with pump-probe delay. (a) The raw PA amplitude of an object at different delay between pump and probe. (b) The transient absorption extracted from the photoacoustic measurement with two oxygen level.

1.3 Photoacoustic lifetime imaging (PALI)

While the photoacoustic pump-probe approach is able to measure oxygen concentration with location information in terms of distance from the transducer, it can only provide a 1-D profile of oxygen distribution. In order to map the oxygen distribution with additional dimension, another degree of freedom is added. An approach is to move the ultrasound transducer with respect to the objects, so that from the ultrasound, different location can be revolved. In the case showing in Fig. 5(a), a focused ultrasound transducer is translating, thus detecting ultrasound only within its focused region and eliminating interference. Similar to B-mode ultrasound imaging, amplitude lines are stacked with position information to form a 2-D image of photoacoustic image, as shown in Fig. 5(b), the lifetime is then extracted on a pixel-by-pixel basis.

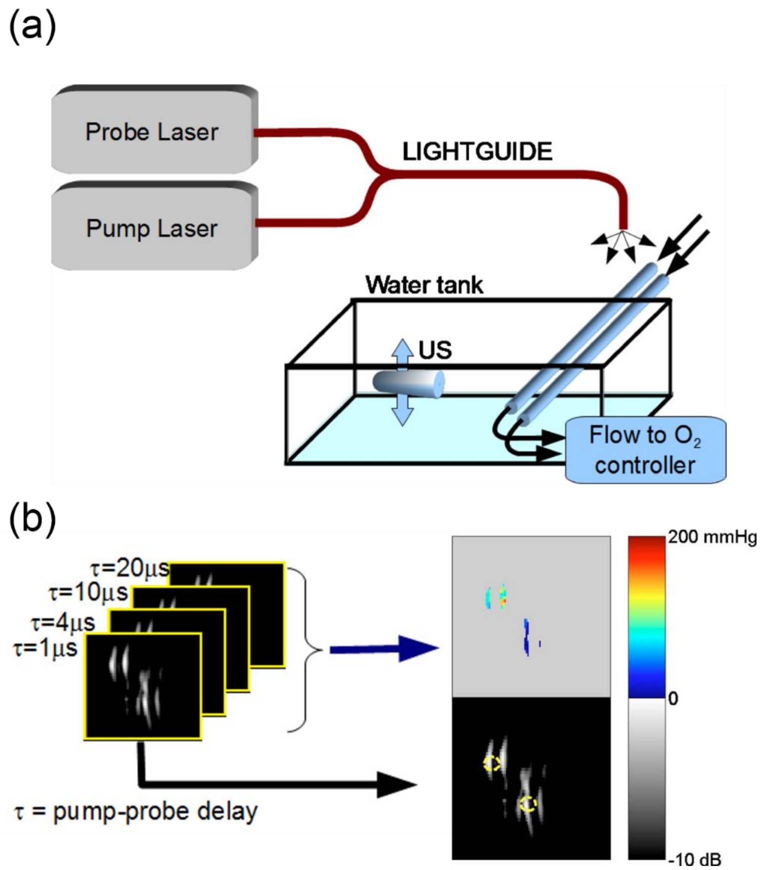

Figure 5 2-D photoacoustic lifetime imaging performed by translating ultrasound transducer, adapted from [Ashkenazi 2010]. (a) PALI imaging experimental setup. The setup includes a pulsed pump laser (650 nm), pulsed probe laser (808 nm), and a light guide that combines both laser outputs and illuminates the phantom object. An ultrasound (US) transducer (10 MHz, focused) mounted on a motorized stage collects the PA signals. The phantom includes two plastic tubes. Two separate closed flow loops control independently the oxygen level dissolved in MB dye solution in each tube. The phantom and ultrasound transducer are immersed in a water tank. (b) (Top) PALI image of the two-tubing phantom. Color code indicates oxygen partial pressure in mmHg. Areas where pO_2 cannot be resolved due to low photoacoustic signal are represented by light gray. (Bottom) Photoacoustic amplitude image in decibel grayscale. Front and back sides of each tube appear as a double spot in the image (true location of tubes indicated as yellow dashed circle).

Translating ultrasound transducer is capable of generating 2-D PALI images, however the temporal resolution is largely limited by the mechanical motion of the transducer. In order to image an object within a few minutes scale, an ultrasound array is applied. An ultrasound array is made up of multiple ultrasound transducers arranged in a fixed pattern. The key concept of applying more transducers can be illustrated in Fig. 6. An object in the field of view can be detected by more than one ultrasound transducer when generating photoacoustic waves. The distance from the object to all the ultrasound transducers provides addition information of its position, thus enable possibility of reconstructing the acoustic source by solving inverse problems.

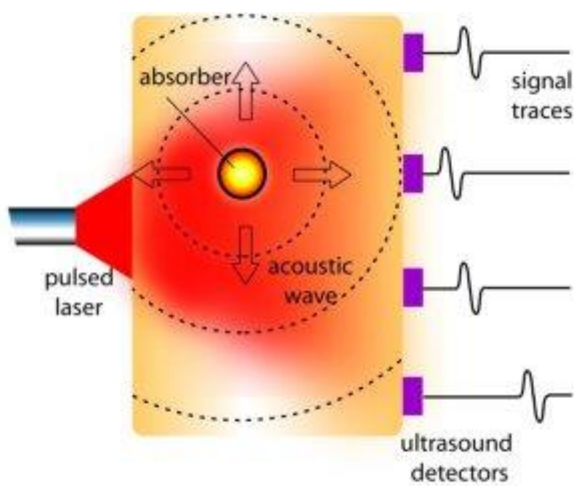

Figure 6 Photoacoustic signal can be detected by multiple ultrasound transducer simultaneously. [13]

A multi-modal imaging system is constructed to allow for three modes of operation: pulse-echo US imaging, photoacoustic imaging, and PALI. Both lasers (pump and probe) are externally triggered by an FPGA module, so that both the pump and probe operate at a 10 Hz repetition rate. The FPGA module also generates a time delay between pump and probe. In our imaging example, the time delay is controlled by a PC via the parallel port.

The FPGA also sends triggering signal to the open system so that the data acquisition starts immediately after the laser pulse. The clock for the FPGA is halved from internal clock (80 MHz) of the open system, which synchronizes both the ultrasound pulse generator and AD conversion of signals received from the ultrasound probe. The open system is connected to a 64-channel ultrasound phased array for emitting and receiving ultrasound. The amplification gain of channels can be programed from 0 to 79.9 dB. The data are stored and then transferred to the PC for imaging processing.

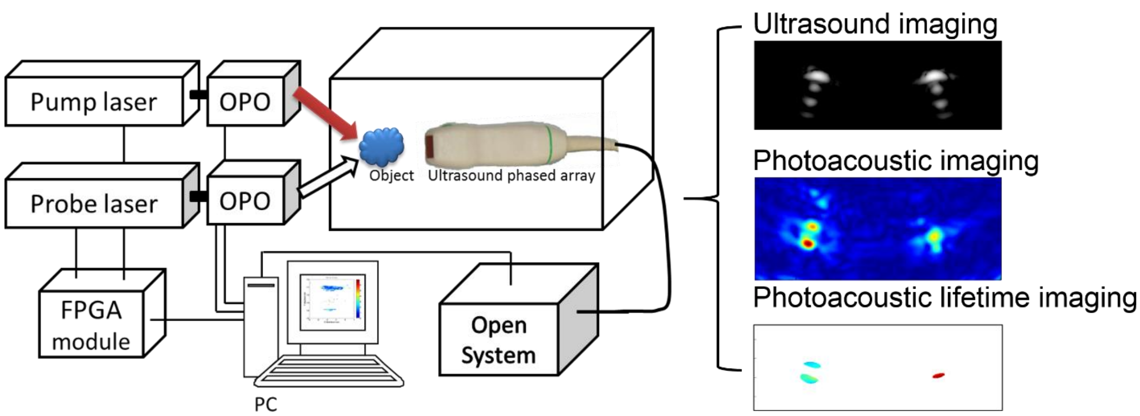

Figure 7 The schematic of a multi-modal imaging system.

Ultrasound imaging and PALI modes of operation share the same system setup. In ultrasound imaging mode the lasers are turned off. The open system is set to internally triggered (without control from the FPGA), which synchronize only the ultrasound pulse emission and echo reception. At each step, only one channel of ultrasound elements on the phased array transducer emits ultrasound pulse, when immediately all channels start to receive the echo. Such step is repeated until echo from every single element is recorded. During the pulse and echo, the digitized data are temporally stored at the memory of the open system. The data are finally transferred to the PC for signal and imaging processing.

When working in PALI mode, the open system is set to external triggering mode, with the ultrasound pulse generator shut down to eliminate any electronic noise. Both lasers and the open system are triggered by the FPGA module. For each laser, there are two triggered event, the flash lamp and the Q-switch. The time delay between them is tuned so that the laser gives maximum output energy.

Chapter 2 In vivo photoacoustic lifetime imaging of tumor hypoxia in small animals

Contributing Authors: Qi Shao, Ekaterina Morgounova, Chunlan Jiang, Jeunghwan Choi, John Bischof and Shai Ashkenazi

The following chapter appeared in publication: Shao et al. Journal of Biomedical Optics 18(7), 076019 (July 2013)

2.1 Introduction

Regions of hypoxia are commonly found in solid tumors. Hypoxia is caused by abnormally low oxygen transport[14] and an imbalance in the supply and consumption of oxygen[15]. Furthermore, tumor hypoxia is strongly linked to a low treatment efficacy in chemotherapy and radiotherapy for several types of human tumors.[16, 17] Hypoxia is also correlated with aggressive tumor phenotype and poor prognosis.[18] Some studies suggest that, tumor hypoxia does not depend on tumor size, grade or extent of necrosis.[19] It has also been shown that tumor oxygenation is not correlated with oxygen saturation of hemoglobin in blood (sO_2).[20] Monitoring oxygen partial pressure (pO_2) in tumors has profound implications for the planning of effective therapeutic strategies[21, 22] and for assessing methods of modulating tissue oxygen to enhance the efficacy of cancer treatments.

The chemical and physical properties of oxygen enable a wide variety of methods for measuring pO_2 *in vivo* by both local and regional methods. Clinically, the gold standard is based on the local computerized polarographic needle electrode method.[23] However, these systems are invasive and not capable of mapping (imaging) the oxygen content in tissue. Characterizing the heterogeneity of oxygen distribution over the region of interest is valuable in investigating the underlying pathophysiology, as well as for making clinical treatments more effective.[24]

This has led to the development of oxygen content imaging methods that can be categorized into three groups: optical, nuclear, and magnetic resonance based. While these methods all provide information about oxygen, they each have significant limitations. Optical methods including near-infrared spectroscopy (NIRS)[25] and phosphorescence imaging[26] suffer from low penetration depth due to the strong optical scattering in tissue. Nuclear methods use various hypoxia-related probes for positron emission tomography (PET)[27] and single-photon emission computed tomography (SPECT)[28]. These radiolabeled compounds indicate activity of cell metabolism, which is not directly related to oxygen content in tissue. Moreover, interpreting the images for identification of hypoxic regions is highly susceptible to time delay between injection of contrast agent and image acquisition.[29] Magnetic resonance based methods include blood oxygen level-dependent magnetic resonance imaging (BOLD MRI)[30], ^{19}F MRI[31], electron paramagnetic resonance imaging (EPRI)[32], and proton–electron double resonance imaging (PEDRI)[33]. BOLD-MRI assesses the hemoglobin oxygen saturation and thus can only serve as an indirect measure of tissue oxygenation. Moreover, all MRI methods have a long scanning time and therefore cannot generate real-time images. Other disadvantages include their high cost and incompatibility with implants and pacemakers. Real-time oxygen imaging is particularly beneficial in photodynamic therapy (PDT) where tissue oxygenation changes significantly during the course of treatment and can serve as a critical factor for understanding the post-treatment metabolic pathway of the tumor.[34] Because of the aforementioned inherent limitations in optical, nuclear, and MRI-based methods, these modalities are not commonly implemented in a clinical setting. This indicates a strong clinical need for a new oxygen imaging modality.

In previous work we have demonstrated the capability of the photoacoustic lifetime imaging (PALI) technique for measuring pO_2 in a phantom.[1, 35] Here we report our first study in extending this method to image pO_2 distribution *in vivo*. PALI has several distinctive features that make it a promising alternative to current clinical pO_2 imaging methods. It relies on local measurement of triplet state lifetime of a chromophore. The lifetime is highly dependent on pO_2 for chromophores having a sufficiently stable triplet state. This contrast mechanism is similar to those of pO_2 imaging methods based on phosphorescence lifetime[1]. The readout penetration depth and resolution, however, are greatly improved in PALI because the excitation lifetime is measured by photoacoustic imaging (PAI), a technique that circumvents the difficulty posed by strong optical scattering in tissue. Specifically, PAI relies on detection and imaging of acoustic signals generated by light absorption of short laser pulses. Its resolution is determined by the ultrasound (US) transducer that is used for photoacoustic (PA) signal detection and therefore resembles that of US imaging.[36, 37] Penetration depth of PAI depends on diffused light penetration in tissue and can reach up to 5 cm.[38, 39]

PALI utilizes two pulsed-laser sources, one for exciting the chromophore and the other for PA probing of the excited state. The first laser pulse pumps the dye to an excited state. The dynamics of relaxation back to the ground state results in transient optical absorption. This transience can be probed by a second pulsed laser that generates PA waves. The amplitudes of these waves depend linearly on optical absorption in the sample. Because the absorption is time-dependent, the amplitudes of the waves change with the time delay between the two pulses. Therefore, by altering this time delay, the decay of the excited state population can be measured and the excited state lifetime can be extracted. The PA signals are detected and then processed to reconstruct a PA image at each pump-probe time delay. The sequence of images is then used to track the decay profile of the excited state independently at each pixel position in the field of view. PALI thus provides an image showing the distribution of the excited state lifetime.

Combining PALI with tissue staining by oxygen-sensitive dye yields a method for tissue oxygen imaging. The oxygen sensitivity of these dyes is based on dynamic quenching of the excited state by collisions with oxygen molecules. High oxygen sensitivity requires that the rate of collisions be higher than the relaxation rate of the excited state. For this reason, long lifetime dyes are preferred for oxygen sensing. Particularly useful are dyes that exhibit efficient intersystem crossing (ISC) to a metastable triplet state. In this case, the lifetime is typically in the microsecond or even millisecond range.

In this work, we chose to use methylene blue (MB) as an oxygen-sensitive dye. MB is a water soluble dye that is widely used in clinical diagnostic and therapeutic applications.[5-7] This is due to its low cytotoxicity and efficient clearance from the body via bile, feces, and urine.[9, 40] In addition, the lifetime of MB is an intrinsic property and does not depend on its concentration (79.5 μs in oxygen-depleted solution[10]). MB is relatively stable in stained tissue for up to several hours. After this period, transport via blood circulation and lymphatic clearing takes place as well as the reduction of MB to its non-absorbing leuco form. Because image acquisition time is typically less than 3 minutes, this time-window of relatively stable dye concentration in the target tissue is long enough to warrant its application in PALI oxygen imaging.

In vivo application of the lifetime-based PA technique has previously been reported by Ray et al..[41] They used G2, a dendrimer-based oxygen-sensitive dye[42], to measure pO_2 in a single point in the main artery of a rat tail. Their measurements were confined to the blood volume because the G2 dye does not penetrate vessel walls due to its relatively large molecular size.[43, 44] In the work presented here, we were able to measure pO_2 in the solid tissue because MB is a small molecule that rapidly stains tissue by diffusion. In order to map the distribution of pO_2 in the solid tissue, a full 2D imaging technique has been implemented.

2.2 Materials and methods

2.2.1 Multimodal imaging system

The schematic of the multimodal system is shown in Fig. 8. The system allowed for three modes of operation: pulse-echo US imaging, PAI, and PALI. The pump laser was a pulsed Nd:YAG laser (Surelite I, Continuum), equipped with a third harmonic generation module, emitting short pulses (5 ns) at 355 nm. An optical parametric oscillator (OPO, MagicPRISM, OPOTEK) was used in conjunction the laser to generate a wavelength of 650 nm to match the peak absorption of MB in its ground state. A frequency-doubled Nd:YAG pulsed laser (Brilliant, Quantel, 532 nm, 5 ns) commercially integrated with a second OPO unit served as the probe laser. The integrated laser system (Rainbow, OPOTEK) provided a tuning range of 680 to 960 nm. The output wavelength of this laser system was tuned to 810 nm to match the excited state triplet-triplet peak absorption of MB. The pulse energies at 650 nm and 810 nm were measured to be 8 mJ and 10 mJ respectively. A set of prisms was used to align the two beams such that they overlapped at the surface of the imaging object. The light intensities of the two beams were approximately 8 mJ/cm^2 and 13 mJ/cm^2, which are below the ANSI limit.[45]

Both lasers were externally triggered by an FPGA module (Saxo FPGA board, KNJN) at a 10 Hz repetition rate. The time delay between the pump and probe pulses was controlled by a PC via a parallel port connection to the FPGA module. The module also triggered the signal acquisition of a 64-channel US system (OPEN system, Lecoeur Electronique). The US system was connected to a 64-element US phased array transducer

(P7-4, ATL). This transducer has 64 elements arranged in a linear array configuration with inter-element spacing of 0.18 mm. The center frequency of the transducer is 5 MHz and its bandwidth is 3 MHz. The same transducer was used as a transmitter-receiver in pulse-echo US imaging mode and as a receiver-only in photoacoustic imaging (PAI) and PALI. All 64 channels were digitized simultaneously at 12-bit resolution. The amplification gain of each channel can be programmed from 0 to 79.9 dB. The data were stored in an internal buffer and then transferred to a PC for image reconstruction and processing. The 80 MHz internal clock of the US system was utilized as a common time-base for all other clocks and triggering signals in the multimodal imaging system, thereby ensuring minimal jitter between laser pulses and PA signal acquisition.

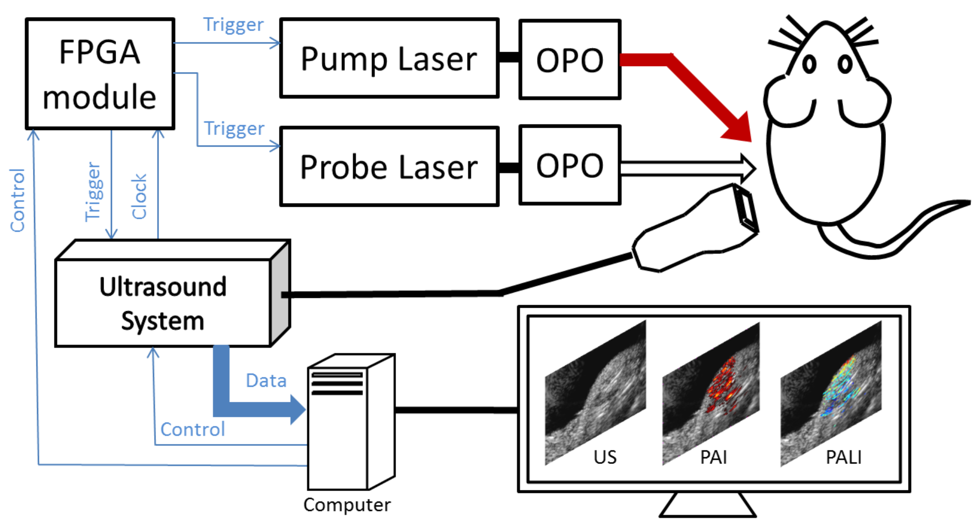

Figure 8 Schematic of in vivo multimodal imaging system. The system was capable of generating US, PAI, and PALI images using the same hardware. The animal was illuminated by two laser systems triggered by an FPGA module. Both pulse-echo US and PA signals were acquired by a conventional phased array US transducer, and then amplified, digitized and stored in the US system. Data were transferred to a PC for image processing and display.

2.2.2 US Imaging

In US imaging mode, the lasers were turned off, and the US system triggering was set to internal. US images were obtained by the synthetic transmit aperture (STA) method.[46, 47] At each step, only one channel of the phased array emitted an US pulse, and the reflected backscattering signals were simultaneously recorded on all 64 channels. This step was repeated until the echo signals from every emitting channel were acquired. The signal acquisition time for a complete scan was less than 100 ms. This method generates a data set from which signals corresponding to any pair of emitting and receiving elements can be extracted. For each emitting element, an amplitude image was reconstructed by the delay-and-sum method[48], followed by Hilbert transformation along the axial direction for conversion to a complex, analytical signal. Finally, all complex amplitude images were summed, and the absolute values were presented using dB scales.

2.2.3 PAI and PALI

When working in PAI and PALI modes, both lasers were turned on, and the US system was then set to external triggering mode with the US pulse generator turned off to reduce electronic noise. The PA signal acquired by the US array was averaged over 100 measurements to compensate for the fluctuations in the OPO output energy. A filtered backprojection algorithm was applied to reconstruct the PA images.[49] The PA signal was filtered by a zero phase-shift FIR filter with bandwidth of 3 - 7 MHz, and then processed through a coherent summation procedure to generate the PA amplitude at each pixel in the field of view. Envelope detection was then applied by taking the absolute value of the Hilbert transform of the PA amplitudes along lines in the depth direction. The final step was required for generating a unipolar PA image.

A series of PA signals was obtained with pump-probe delays (τ) of 0.25 μs, 0.5 μs, 1 μs, 2 μs, 4 μs, 8 μs and 100 ms. The delay was accomplished by changing the time of the pump with respect to the triggering signal to US system. At each delay, PA signals were recorded with the probe beam both on (synchronized with start of US signal acquisition) and off. Taking into account the 10 Hz repetition rate and the time for data transfer, the total imaging acquisition time was approximately 150 seconds. This includes averaging of 100 samples for each PA signal. In order to extract the transient PA signal, the following steps were applied. First, the PA signal corresponding to the 810 nm laser (S_{810}) was calculated by subtracting the PA signal generated by the 650 nm laser only (S_{650}) from the PA signals generated with both lasers (650 nm and 810 nm) emitting ($S_{810+650}$) at a specific pump-probe time delay (τ_0), as described by Eq. 1.

$$S_{810,\,\tau=\tau_0} = S_{650+810,\,\tau=\tau_0} - S_{650,\,\tau=\tau_0} \qquad (1)$$

The S_{810} signal had two independent components, a background absorption signal due to light absorption in tissue (mostly in hemoglobin) ($S_{810,\,background}$), and a transient absorption signal of MB at τ_0 ($S_{810,\,transient,\,\tau=\tau_0}$). The two components were separated using a background suppression method described by Huang et al.[50] and below in more detail. The background absorption is independent of the pump-probe time delay. Therefore the background PA signal was obtained by separating the two individual PA responses (650 nm and 810 nm) at a long τ (100 ms), a value that is much longer than the normal range of lifetime of MB (less than 100 μs). The transient PA signal was then obtained by subtracting the background PA signal at 810 nm from the total PA signal at 810 nm.

$$S_{810,\,background} = S_{650+810,\,\tau=100ms} - S_{650,\,\tau=100ms} \tag{2}$$

$$S_{810,\,transient,\,\tau=\tau_0} = S_{810,\,\tau=\tau_0} - S_{810,\,background} \tag{3}$$

A sequence of PA amplitude images of the transient absorption was then reconstructed from the transient PA signal $S_{810,\,transient,\,\tau=\tau_0}$. Each image in the sequence corresponds to a different time delay. The following set of time delays was used: 0.25 μs, 0.5 μs, 1 μs, 2 μs, 4 μs and 8 μs. For each pixel, the lifetime (T) and the transient PA amplitude (A_0) were computed by fitting the amplitude (A) to an exponential decay function of the pump-probe delay τ.

$$A = A_0 e^{-\frac{1}{T}\tau} \tag{4}$$

Additionally, the coefficient of determination, R^2, was computed at each pixel to reflect the goodness of fit. The amplitude threshold was set to be ¼ of the global maximum amplitude of the PA image. An amplitude above threshold and an R^2 value above 0.8

were used as selection criteria to ensure the validity of lifetime estimates. Only pixels that met both criteria were converted to pO_2 values and displayed in a color scale. The Stern-Volmer relationship (Eq. 5) describing the lifetime as a function of pO_2 [51] was used to convert lifetime to pO_2.

$$T^0 / T = 1 + k_Q T^0 pO_2 \tag{5}$$

Where T^0 is the lifetime at $pO_2 = 0$, and k_Q is the quenching rate constant. For MB T^0 = 79.5 μs, and k_Q = 0.0036 $\mu s^{-1} mmHg^{-1}$.[10]

2.2.4 Phantom imaging

To demonstrate the capability of multimodal imaging, we tested the imaging system using a phantom consisting of two tubes. The experimental setup is shown in Fig. 9(a) and Fig. 9(b). Two plastic tubes (inner diameter of 0.7 mm, outer diameter 2.4 mm) containing MB aqueous solution at different pO_2 were placed perpendicular to the scanning plane. The solution in each tube was in closed-flow circulation with an oxygenation cell, in which the pO_2 level was controlled by gas bubbling. One cell was bubbled by air so that the pO_2 of the solution is air-equilibrated, and the other one was bubbled by pure nitrogen. The US transducer was placed near the tubes, with both lasers illuminating the tubes from the side (left side of Fig. 9(a)). Both PA and US signals were recorded without moving the tubes and transducer. PA images at a series of time delays were reconstructed, and the lifetime was extracted and converted to pO_2 for display.

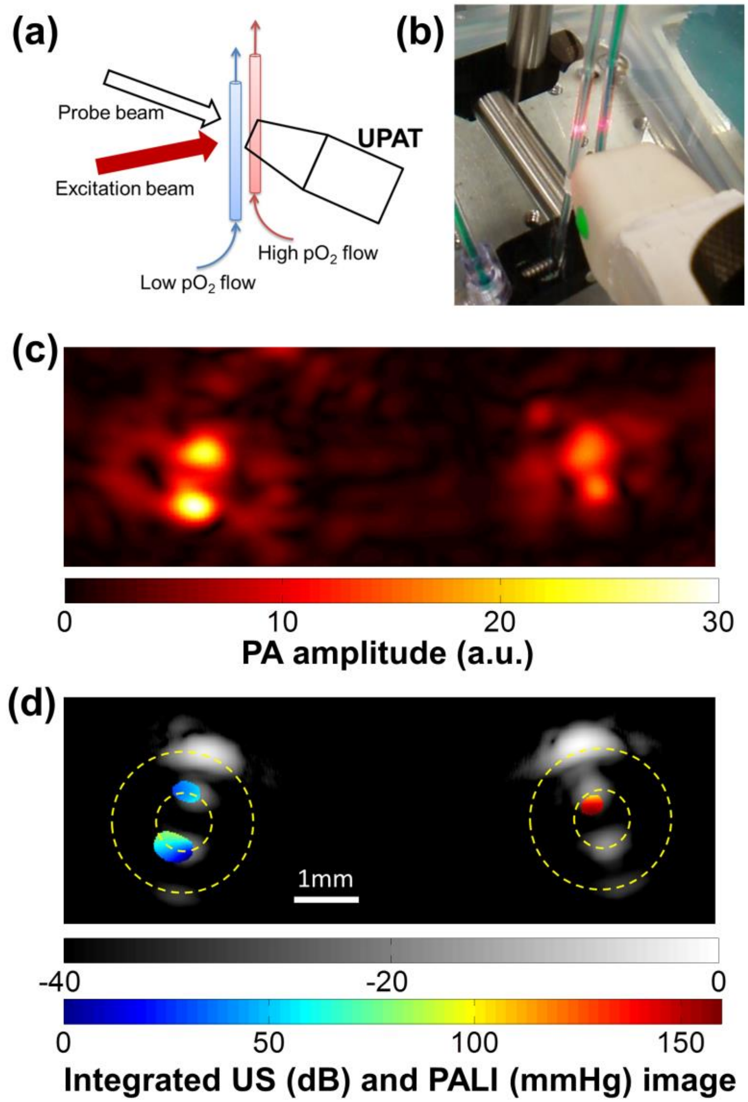

Figure 9 Experimental setup and multimodal imaging results of a two-tube phantom experiment. (a) The phantom consisted of two plastic tubes containing MB aqueous solution at high pO_2 (150 mmHg, right) and low pO_2 (50 mmHg, left). Both tubes were illuminated by the excitation beam (650 nm laser) and probe beam (810 nm laser). (b) Photo of the phantom and the US transducer. UPAT, ultrasound phased array transducer. (c) Transient PA image of the two tubes by the 810 nm laser at a pump-probe delay of 0.5 μs displayed in a linear scale. The two clusters of PA signals represent the location of the wall-dye interface in the two tubes. The phantom was illuminated by two lasers from the left, resulting in higher PA amplitude in the left tube. (d) PALI image (color) superposed on US (gray scale) image. Inner and outer walls of both tubes are indicated by dashed lines.

2.2.5 Animal preparation

Tumor-bearing nude mice were used as a cancer model in this study. Tumors were induced by injecting LNCaP cells into the hindlimbs. The LNCaP cell line was derived from human prostate adenocarcinoma and has been commonly used in cancer research.[52-54] Specifically, 1×10^6 cells suspended in 0.1 ml of matrigel matrix (50% of Matrigel and 50% of LNCaP growth medium) were subcutaneously injected into the hindlimb of each 24 gram nude mouse. Tumors grown for 3 – 5 weeks with a diameter of 5 – 10 mm were considered appropriate for further experiments.

MB (methylene blue hydrate, Fluka) was dissolved in physiological saline (DPBS 1X, Mediatech) to a concentration of 5 mM. After the animal was anesthetized by ketamine (100 mg/kg) and xylazine (10 mg/kg), the MB solution was injected into the hindlimb. The amount of MB injection was 0.2 - 0.6 ml at each spot (5 - 10 mm between injection spots, total injection volume was limited to 1 ml for a given hindlimb). Data acquisition was initiated after 10 - 15 min to allow the dye to sufficiently diffuse in the tissue. All animal procedures and care were performed according to protocols approved by the University of Minnesota Institutional Animal Care and Use Committee in accordance with federally approved guidelines.

2.2.6 In vivo oxygen imaging and measurement

The animals were divided into two groups: mice with hindlimb tumor (group A, n_A=8), and control non-tumor bearing mice (group B, n_B=10). Two animals from each group were randomly chosen for imaging, while the rest were used for direct measurements using an oxygen probe for comparison. In group A, both the PALI and oxygen probe were applied to quantify the pO_2 of the tumor and normal tissue at the hindlimbs. In group B, pO_2 of the non-tumor bearing hindlimb of control mice were measured by both methods. The pO_2 values in PALI were obtained from individual pixel values within regions of interest in the images, while the pO_2 values by the oxygen probe were directly recorded. The statistics of pO_2 values obtained by PALI and the probe with 3 types of tissues (tumor tissue, normal tissue and control mice) were compared.

The animal chosen for imaging was transferred to the imaging platform as shown in Fig. 10. The imaging platform included an animal holder in order to keep the hindlimb of the animal submerged in water and the head above the surface for normal breathing. The transducer and platform were fixed by mechanical arms so that the relative position of the animal and US transducer did not change throughout the experiment. The water temperature was kept at 35 $\pm$ 0.5 ℃ by a digital heating system (T3-150, Transworld Aquatic Enterprises). US images were generated to provide the anatomical structure of the hindlimb. PA images at each pump-probe delay were obtained and then processed to yield the PALI image. After the imaging procedures, the animal was euthanized.

To perform direct oxygen measurements, the animal was first anesthetized and transferred to a heater pad. The pO_2 of the hindlimb was then assessed by a commercial single-point oxygen probe. The device consists of a retractable needle-type oxygen sensors (sensor tip diameter 50 μm, surrounded by a 40 mm long and 0.8 mm wide syringe needle, OXR50, Pyroscience) and optical oxygen meter (Firesting O_2, Pyroscience). The Firesting O_2 system is a PC-controlled fiber-optic oxygen meter that measures pO_2 by quantifying the oxygen-dependent phosphorescence of a dye-stained polymer membrane located at the tip of the optical fiber. The oxygen sensor was inserted into tissue with the needle. By pulling out the probe in a step-wise manner, pO_2 values along the needle path at different depths were recorded. Typically, three needle penetrations were made in one hindlimb, and 2 - 4 stable pO_2 readings were recorded for each penetration. The animal was euthanized after the measurements.

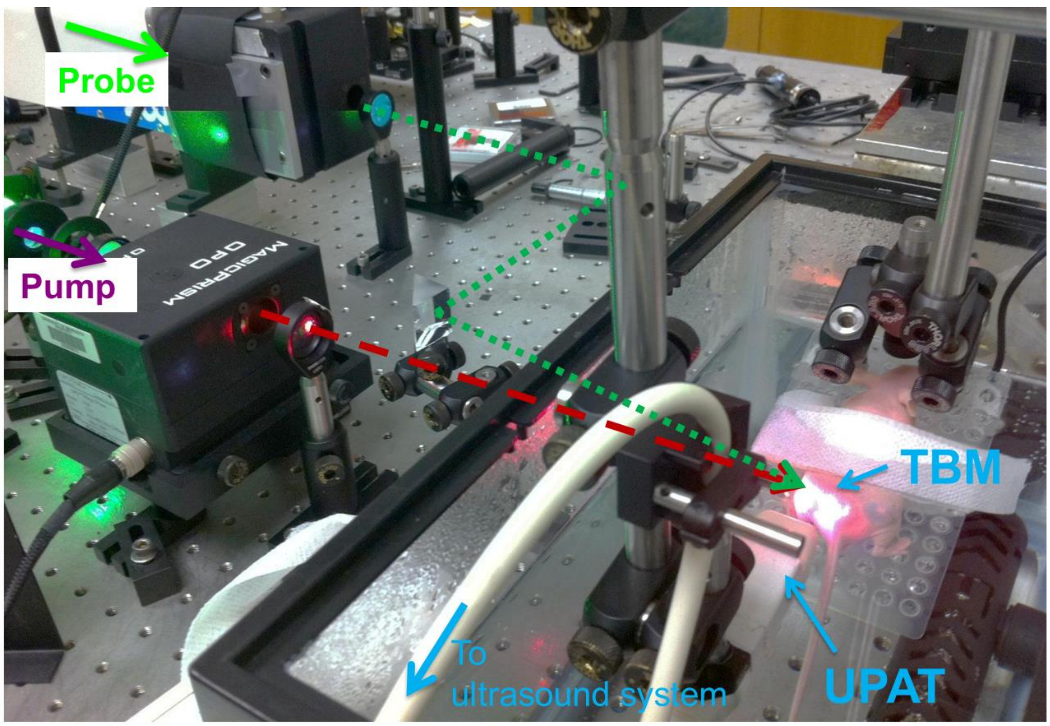

Figure 10 In vivo imaging platform for small animals. The nude mouse was fixed within a water tank with its head above the water level. Two laser beams overlapped on the tumor-bearing hindlimb, while the US transducer was positioned next to the illuminated spot and aligned for multimodal imaging. TBM, tumor-bearing mouse; UPAT, ultrasound phased array transducer. Red dashed line, the 650 nm laser beam; green dotted line, the 810 nm laser beam.

2.3. Results

2.3.1 Phantom imaging

An example of multimodal imaging results of a phantom is given in Fig. 9(c) and Fig. 9(d). Fig. 9(c) shows the PA image of the phantom. Fig. 9(d) shows the superposition of the PALI image onto the US image. Both the PA and US images correctly reflect the structure of the phantom, with the PA image showing the optical absorption of the contents inside the tubes and the US image indicating the inner and outer walls. The different levels of pO_2 in the two tubes are shown in the PALI image. The pO_2 within the left and right tubes were set to 50 and 150 mmHg respectively. The PALI image clearly shows levels in the range of 40 - 60 mmHg and 130 - 160 mmHg for the left and right tubes, respectively.

2.3.2 In vivo imaging

The setup for the *in vivo* measurements is shown in Fig. 10. PA images and PALI images were superposed onto the US image. As can be seen from Fig. 10, the laser beams illuminated only a portion of the hindlimb due to the limited power of the lasers. Therefore, both PA and PALI images covered less area than the US image (Fig. 11(a)). The PA image shows the amplitude distribution resulting from the background absorption (Fig. 11(b)) and MB's transient absorption (Fig. 11(c)). The transient PA amplitudes associated with two pixels, along with their exponential decay determined by curve-fitting, are shown in Fig. 11(e). The two pixels correspond to points with high and low

pO_2 respectively. The hypoxic region imaged by PALI (Fig. 11(d)) is consistent with the site of the tumor imaged by US. We have also applied the same technique to the control mice without tumor. The PALI images indicate inhomogeneous tissue oxygenation within the normal muscle tissue, and the pO_2 values were within the normal physiological range.

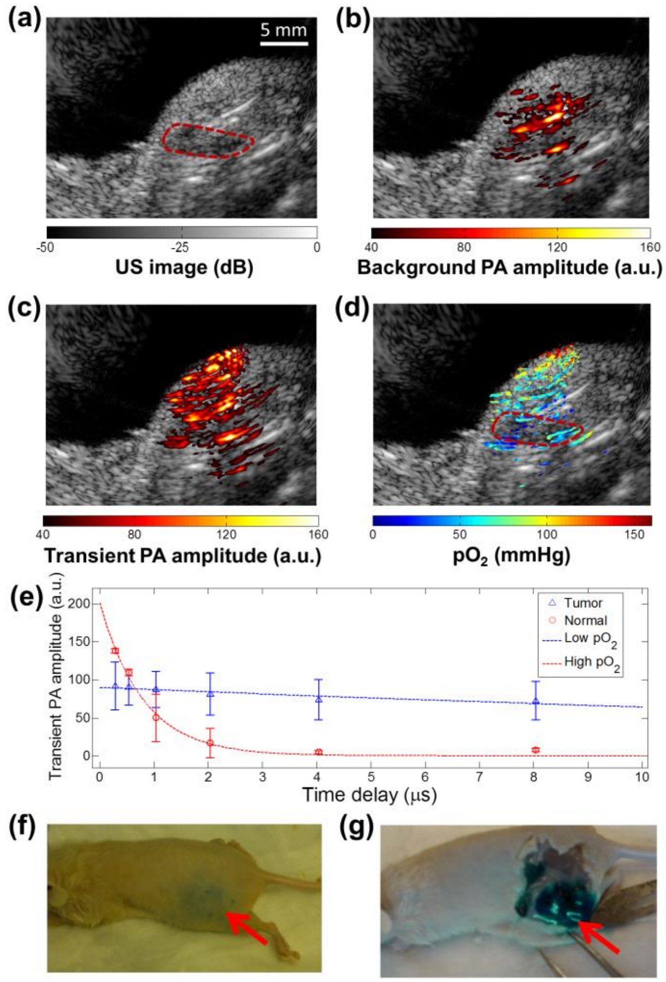

Figure 11 Multimodal imaging of the tumor-bearing mice. (a) US image of the left tumor-bearing hindlimb of a mouse. The area of the tumor is enclosed by a red dashed line. (b) PAI representing the amplitude of background absorption at 810 nm. Amplitude is displayed in linear scale. (c) PAI of the transient absorption of MB with an 810 nm laser at a pump-probe delay of 0.25 μs. (d) PALI of pO_2 in color scale

superimposed on US image. (e) Transient PA amplitudes of two representative pixels within the tumor and in normal control tissue respectively. The triangles and circles are the averaged transient PA amplitudes of tumor and normal control tissue respectively. The error bars represent the standard deviation of 100 recordings. Both sets of data were fit with an exponential curve as shown by the dashed line. (f) Animal after imaging procedure. An arrow indicates the MB stained imaging region. (g) Open-skin view of the tumor site. Note that the tissue was still stained with MB after the imaging process, thereby confirming stable MB staining of the tissue for a period of more than 1 hour. The red arrow indicates the site of the tumor.

2.3.3 Correlative in vivo measurement

We have performed correlative direct measurements using the oxygen needle sensor in tumor-bearing mice and control mice. The total number of valid pO_2 readings for tumor tissue, normal tissue of tumor-bearing mice, and control mice was 38, 39, and 121, respectively. The three groups of measurements were then compared with the pO_2 values extracted from PALI images. The frequency distributions of the pO_2 values are displayed in a histogram shown in Fig. 12(a). The 3 regions for statistical analysis of pO_2 distribution via PALI are labeled in Fig. 12(b) and Fig. 12(c). We performed two-sample t-tests. The results show a statistically significant difference in pO_2 distribution between tumors and other tissue, with p values below 0.05 by both PALI and the needle probe. Both PALI and direct oxygen measurements confirmed that the tissue oxygen level in the tumors is significantly lower (about 20 mmHg) than that in normal tissue and control mice.

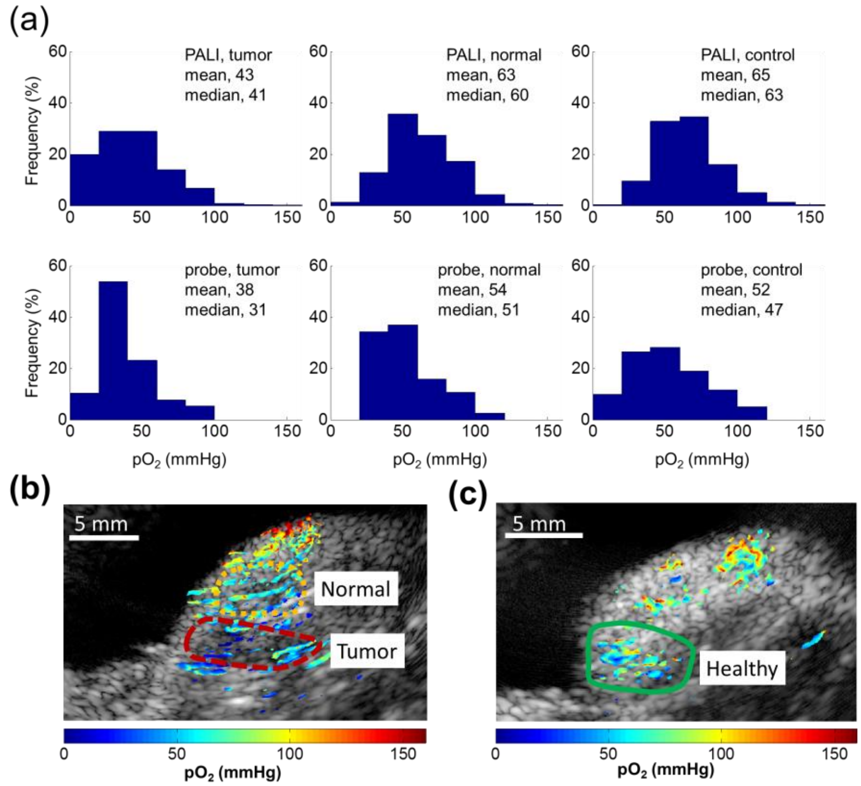

Figure 12 Histogram of pO_2 in tumor tissue, normal tissue and control mice. (a) Top row: histogram of pO_2 values extracted from PALI. Bottom row: histogram of pO_2 values measured by the oxygen probe. Data from tumor tissue, normal tissue (adjacent to tumor site), and control tissue (no tumor present) are displayed in left, middle, and right columns respectively. (b) PALI showing the regions of tumor (red dashed line) and normal (yellow dashed line) sites in a tumor-bearing hindlimb of a mouse. (c) PALI showing the control tissue of a tumor-free hindlimb. The image does not show a substantial area of low pO_2 as compared to Fig.11 (d).

2.4 Discussion

Tissue pO_2 is a key regulator of physiological function, and changes in tissue oxygenation play a critical role in the pathophysiology of a wide range of diseases. In cancer, particularly, low pO_2 in tumors indicates poor prognosis and low efficacy of radiotherapy and chemotherapy. Imaging of pO_2 can significantly improve the quality of diagnosis and treatment planning for cancer patients. Nevertheless, current imaging modalities fail to provide a suitable clinical solution.

In this work, we have demonstrated the *in vivo* application of PALI for tissue oxygen imaging in small animals. PALI is a novel and alternative method for *in vivo* oxygen imaging with the advantages of rapid image acquisition, involving non-ionizing laser radiation, and using a non-radioactive optical contrast agent. In this work, we used MB, a dye that has been widely used in therapeutic and diagnostic applications. The imaging results confirm the existence of hypoxic area caused by the solid tumor. The statistical distribution of pO_2 was compared to direct measurements by an optical needle sensor system. An overall shift toward higher pO_2 values in PALI compared to direct measurements was found. This may have resulted from the higher body temperature during PALI imaging (water temperature of 35 ℃) vs. needle sensor measurements (room temperature of 22 ℃), which might affect blood circulation and tissue oxygenation.

To achieve these measurements a multimodal (US imaging, PAI, PALI) imaging system has been developed. All three imaging modes share the same US transducer, thereby eliminating the need for image co-registration of anatomical and functional information. The system employs a commercial 64-element phased array US transducer. It is optimally designed for clinical US imaging in applications such as echocardiography where limited aperture is required.

The limitations imposed by the limited bandwidth and aperture size compromise accurate reconstruction of large scale structures. The problem of implementing PAI using US imaging arrays has been investigated by several groups.[55-57] These studies show that PA images can still adequately represent tissue structure and morphology by relying on differences in small scale structure of different tissue types, and on the high visibility of interfaces causing abrupt gradients in optical absorption.

The phantom imaging results demonstrate that the system was able to achieve pO_2 distribution of submillimeter structures. Based on the resulting *in vivo* PALI images, the maximal imaging depth of the system is estimated to be about 12 mm. The imaging depth is expected to be improved by increasing the laser energy density. The images also show lack of continuity in the field of view. The regions of valid PALI data consist of isolated "islands" in the field of view. This is mostly a result of low intensity of the excitation laser pulse resulting in low excitation efficiency. This limitation is primarily due to the finite penetration depth of the excitation light in tissue.

One of the advantages of sensing oxygen via PA lifetime is its robustness to large variations in the concentration of the oxygen-sensitive dye and in the intensity of the light. However, low concentrations of the dye and inadequate fluence rate both contribute to a reduction in SNR, making oxygen measurement less accurate. An additional source of noise is attributed to the fluctuations in the pulse energy of both the pump and probe laser. A set of criteria has been developed and implemented to validate the oxygen information. These criteria include a high PA amplitude level and a high R^2 value for exponential fit used for evaluating lifetime.

The results presented here indicate that PALI can be used for mapping tissue oxygen *in vivo*. Furthermore, the work demonstrates the technical capability of multi-modality imaging (US, PAI, and PALI) and its usefulness in visualizing functional imaging data. The technique is very attractive for a range of clinical applications in which tissue oxygen mapping would improve therapy decision making and treatment planning. Examples include cancer treatments (radiotherapy and photodynamic therapy) and treatments of diabetes related ulcers. A more comprehensive validation study of PALI is still required before its implementation in clinical applications could be established. In addition, other methods of light delivery such as the use of minimally-invasive, tissue-penetrating fiber diffusers should be explored in order to extend the applicability of PALI into an even broader range of clinical applications.

2.5 Acknowledgements

The authors would like to thank Mr. Clay Sheaff for his close reading of the manuscript and valuable comments. This work was sponsored by National Institutes of Health grant R21 CA135027.

Chapter 3 Photoacoustic lifetime imaging for direct in vivo tissue oxygen monitoring

Contributing Authors: Qi Shao and Shai Ashkenazi

The following chapter appeared in publication: Shao et al. Journal of Biomedical Optics 20(3), 036004 (March 2015)

3.1 Introduction

In the human body, oxygen is transported from the lungs into the cells via the bloodstream. Oxygen plays a vital role in cellular metabolism. Oxygen partial pressure (pO_2), which results from the balance between oxygen delivery and its consumption, is a key component of the physiological state of tissue. Any imbalance in the oxygen levels, which may occur due to an altered supply or utilization of oxygen, will affect metabolic homeostasis and may lead to diseases[58]. Decrease in pO_2, *i.e.* hypoxia, is strongly associated with diseases such as cancer[59], peripheral artery disease (PAD)[60], diabetes[61], and stroke[62]. The interaction between the availability of oxygen and cellular function, including the signaling pathway of HIF (Hypoxia-inducible factor), has been studied intensively[63]. In medicine, tissue oxygen is essential for diagnosis, therapy planning, and treatment monitoring for a range of diseases [24, 64, 65].

The importance of tissue oxygen characterization raises the need for reliable measurement methods. Images of oxygen distribution may provide information about tissue hypoxia and evidence of oxygen availability in the circulatory system. Tissue oxygen can be assessed either indirectly or directly. Indirect methods include the measurement of oxygen saturation, or parameters related to cell metabolism. Oxygen saturation can be obtained using techniques such as near-infrared spectroscopy[66] and BOLD-MRI[67]. However, tissue oxygenation can be uncorrelated with blood oxygenation when there is insufficient blood perfusion, such as in solid tumors[20] and implantations[68]. Even though numerous hypoxia-related probes used in positron emission tomography (PET)[27] and single-photon emission computed tomography (SPECT)[69] have been developed, the interpretation of the images for identification of hypoxic regions remains highly susceptible to time delay between the injection of a contrast agent and image acquisition [70]. The chemical and physical properties of oxygen enable a wide variety of direct methods for measuring pO_2 in vivo. Polarographic oxygen electrodes[71] and fiber optic probes[72, 73] have been used in clinical practice. These probes are invasive and not capable of mapping (imaging) the oxygen content in tissue. Optical imaging methods including fluorescence quenching[74] and phosphorescence imaging[75] suffer from low penetration depth due to the strong optical scattering in tissue. Magnetic-Resonance-based methods (e.g. ^{19}F MRI[76], electron paramagnetic resonance[32], and proton–electron double resonance imaging[33]) have long scanning times and therefore cannot generate real-time images. Moreover, other disadvantages including high costs and incompatibilities with implants and pacemakers make Magnetic-resonance-based methods rarely implemented in clinical settings.

Evolved from phosphorescence lifetime imaging, photoacoustic lifetime imaging (PALI) is a novel method that directly reflects the spatial and temporal distribution of tissue oxygen [12]. PALI maintains the reliable sensing mechanism of oxygen-dependent decay after excitation. Instead of probing the transient optical emission, which is used in a range of commercially available medical and biological devices[77-79], PALI quantifies the same lifetime from excited state to ground state by probing the transient absorption[35, 41]. The sensing depth of lifetime imaging is thus largely increased by applying photoacoustic imaging. Photoacoustic imaging overcomes the diffusion limit of traditional optical methods by detecting ultrasound generated from light absorption[80]. Penetration depth of photoacoustic imaging in tissue can reach up to a few cm[39]. By combining lifetime oxygen sensing and photoacoustic imaging, PALI is able to reveal the distribution of pO_2 with the resolution determined by an ultrasound transducer, typically less than 1 mm, and a penetration depth of about 15 mm [81-83]. Even though lifetime-based photoacoustic methods enable direct measurement of pO_2, they require perfusion of exogenous contrast agents into the region of interests, which may raise concerns such as biosafety and biocompatibility [70]. In comparison, spectroscopy-based photoacoustic imaging methods quantifying the oxygen saturation (SO_2) rely solely on hemoglobin as an endogenous contrast agent [84-86]. These methods are easier to implement, however they are insensitive to changes in oxygen transport and consumption in tissue. Poor correlations between oxygen saturation and tissue hypoxia have been observed in studies of prostate cancer[87], breast cancer[88], and rectal cancer[89]. These observations strongly suggest that there is a need for imaging methods that directly map tissue oxygen.

We have recently demonstrated the application of PALI to the imaging of tumor hypoxia in a small animal model[81]. The basic principles of PALI have been discussed in greater detail there. PALI consists of a series of excitation–probing pulse pairs. The pump pulse excites an oxygen-sensitive dye, and the probe pulse generates photoacoustic signals proportional to the transient absorption of the dye. These photoacoustic signals are recorded by an ultrasound array. The data acquired following each probing pulse is used to reconstruct a transient photoacoustic image corresponding to a specific pump-probe delay. The series of photoacoustic images are processed in a pixel-wise manner to extract the dynamics of transient absorption at each pixel location in the field of view. Pixel values at different time delays are fitted to an exponential decay function, and decay rates at each pixel are extracted and converted to pO_2 values using the Stern-Volmer equation [90, 91]. The pO_2 values of all pixels are then presented as a pO_2 distribution map. Data validation criteria have been defined to reject unreliable measurements. These include a threshold signal amplitude and a coefficient of determination of the exponential fit.

We use an oxygen-sensitive dye, Methylene Blue (MB), in our work. MB is a water-soluble dye that is widely used in clinical diagnostic and therapeutic applications [92, 93] primarily due to its low cytotoxicity and efficient clearance[8, 9]. MB has several advantages over other oxygen-sensitive dyes: (1) The safety and toxicity of MB in humans has been widely studied and is well documented, including an extensive formal toxicity study by the National Toxicology Program (NTP)[94]; (2) MB can be efficiently (quantum yield for intersystem crossing η_{ISC}=0.52) excited, and the excitation and probe wavelengths (650 nm and 810 nm) lie within the tissue optical windows; (3) the lifetime of MB is an intrinsic property and does not depend on its concentration (79.5 μs in oxygen-depleted solution[10]); (4) the lifetime is highly sensitive to pO_2 (the rate of collisions is higher than the relaxation rate of the excited state) and (5) it has been demonstrated that MB can be used as a photosensitizer in photodynamic therapy (PDT) to treat tumors, which would enable integration of PALI tissue oxygen monitoring with PDT.

3.2 Materials and Methods

3.2.1 Multimodal Imaging System

The imaging system allowed for three modes of operation: pulse-echo ultrasound imaging, photoacoustic imaging, and PALI. The main components of this system were two laser modules, an ultrasound system, and a computer, as shown in Fig. 13. The pump laser generated a wavelength of 650 nm to match the peak absorption of MB in its ground state to excited state transition. The pump laser system combined a pulsed Nd:YAG laser (Surelite I, Continuum), a third harmonics generation module and an optical parametric oscillator (OPO, MagicPRISM, OPOTEK). The output wavelength of the second laser (probe laser) system was tuned to 810 nm to match the excited state triplet– triplet peak absorption of MB. The probe laser (Rainbow, OPOTEK) was a commercially integrated frequency-doubled Nd:YAG pulsed laser (Brilliant, Quantel) with an OPO unit. Both lasers operated at a 10 Hz repetition rate, with a pulse width of 5 ns and pulse energy of about 8 mJ. Light was combined and focused by a series of lenses and mirrors. Light intensities at the illumination spot were between 10-15 mJ/cm^2 (below the ANSI limit[45]). Both lasers were externally triggered by a field-programmable gate array (FPGA) module (Saxo FPGA board, KNJN). The ultrasound system (OPEN system, Lecoeur Electronique) was connected to a 64-element ultrasound phased-array transducer (P7-4, ATL) as a transmitter–receiver in pulse-echo ultrasound imaging mode and as a receiver-only in photoacoustic and PALI modes. In all modes, signals from all channels were simultaneously digitized at a 12-bit resolution at a rate of 80 MHz.

Ultrasound images were obtained using the synthetic aperture imaging method[46, 47], described in[81]. The total signal acquisition time for a complete scan was <1 s. Ultrasound images were generated to provide the anatomical structure of the hindlimb. The photoacoustic signal acquired by the ultrasound array was first averaged over 50 measurements to compensate for the fluctuations in the OPO output energy. A filtered back-projection algorithm was applied to reconstruct the photoacoustic images [80, 95]. A series of photoacoustic signals was obtained with pump-probe delays of 0.25 μs, 0.5 μs, 1 μs, 2 μs, 4 μs, 8 μs and 100 ms. The triplet state lifetime was evaluated at each pixel by an exponential fit. The Stern-Volmer relationship[51] describing the lifetime as a function of pO_2 was used to convert lifetime to pO_2. Data validation criteria have been defined to reject unreliable measurements. These include a threshold signal amplitude (>10% of maximum) and a coefficient of determination (R^2>0.4) of the exponential fit. Only pixels that pass both criteria were shown in the final pO_2 map.

Normal mice (BALB/CJ, The Jackson Laboratory) were used for imaging. Before imaging, mice were anesthetized by ketamine (100 mg/kg) and xylazine (10 mg/kg). Hair on one side of the hindlimb was shaved and removed. Methylene blue (5 mM, about 5 spots, 50μL each spot) was injected subcutaneously at the hindlimb. The mouse was placed in an animal holder, with a lab-made breathing apparatus mounted on the head to allow for free breathing. The breathing apparatus was connected to the flow-rate controller which mixes oxygen, nitrogen and air. The concentration of oxygen inhaled by the animal was achieved by tuning the flow rate ratio of either oxygen or nitrogen with respect to the air. The total flow rate stayed at 120 ml/min for the entire experiment. Imaging experiments were conducted 15 min after the dye injection to allow for sufficient dye distribution in the tissue by diffusion. The pO_2 of the hindlimb was also assessed by a commercial single-point oxygen probe. The device consisted of a retractable needle-type oxygen sensor (OXR50-OI, Pyroscience) and optical oxygen meter (Firesting O2, Pyroscience). The needle was placed close to the imaging area in order to obtain a simultaneous recording of the tissue, but also to avoid direct laser exposure and damage the optical sensing tip, as shown in Fig 13 and Fig 14(d). All animal procedures and care were done using protocols approved by the University of Minnesota Institutional Animal Care and Use Committee (IACUC) in accordance with federally approved guidelines.

Three PALI images were taken under the condition of breathing in 21%, 80% and then 10% of oxygen, with ultrasound images capturing the structure and without touching the mouse. For each condition, imaging started 1 min after switching conditions, so that the mouse was able to adjust to the new condition to ensure physiological stability during imaging. To avoid impairment of the animal's health the total time of exposure to each gas mixture was limited to 4 minutes. After three imaging processes, the breathing tool was removed, and the mouse recovered from anesthesia in the open air and on a heat pad. The health status of the animal was monitored after the experiment, and no side effects were observed.

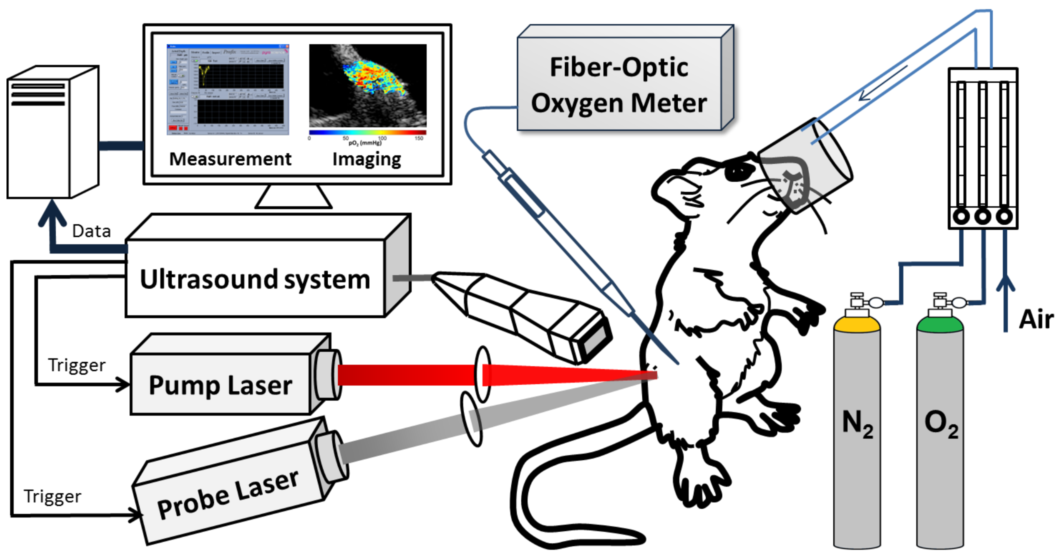

Figure 13 Schematic of in vivo multimodal imaging system and breathing modulation model. The imaging system is capable of generating ultrasound, photoacoustic imaging, and PALI images using the same hardware. Two lasers illuminate the intended target region of the animal, and the generated ultrasound signals are acquired by a phased-array ultrasound transducer and then amplified, digitized, and processed in an ultrasound system. The percentage of oxygen the mouse inhales is controlled and the tissue oxygen near the imaging area is measured during the imaging process.

3.2.2 Ischemia model

The same species of mice was used in this model. The animal was put on the same imaging platform and anesthetized as described in the breathing model. A PALI image was first taken under a normal condition. After the mouse under a normal physiological condition was imaged, acute ischemia of the hindlimb was induced by tightening a rubber band on the proximal side of the hindlimb, thus creating a localized ischemic condition on sites distal to the site of the occlusion. A second PALI image was taken under the ischemic condition. Immediately after the second image, the rubber band was removed, and a third PALI image was taken to capture the condition of reperfusion. The animal was under each condition (namely normal, ischemic, and post-perfusion) for less than 20 min (including about 10 min of the imaging time).

3.3 Results

3.3.1 Breathing modulation

PALI is able to reflect the change of oxygen level with respect to both oxygen-rich (80% O_2) and oxygen-poor (10% O_2) conditions to the normal oxygen level (21% O_2) in the air, as shown in Fig. 14. A high percentage (80%) of inhaled oxygen resulted in higher tissue oxygen levels. Furthermore, a low oxygen percentage (10%) resulted in hypoxic tissue. Both changes due to modulated inhalation are shown in Fig. 15. The PALI results were consistent with the oxygen probe single point measurement.

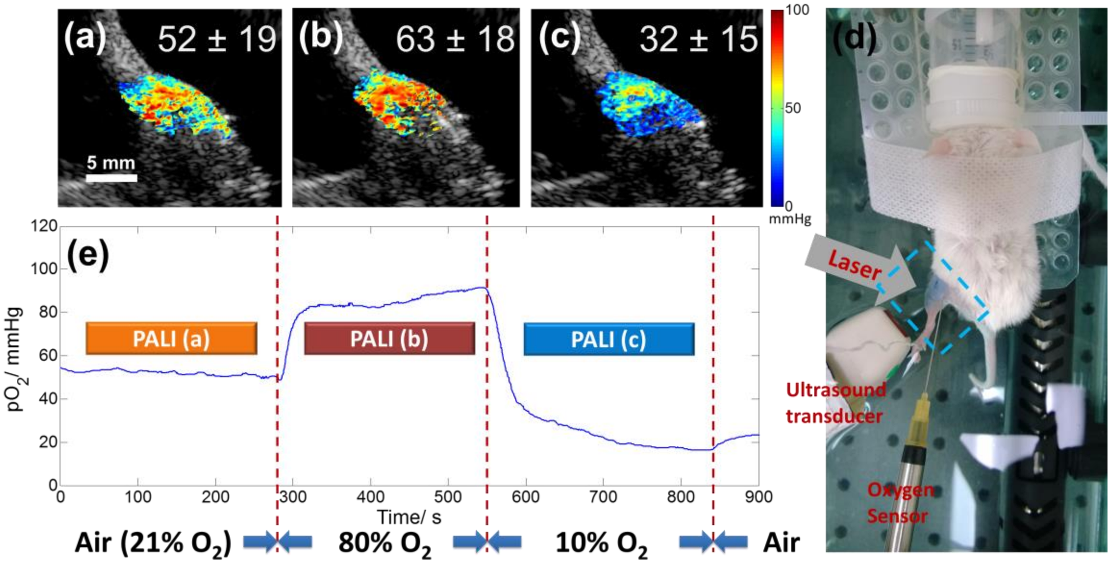

Figure 14 PALI tracking of pO_2 during breathing modulation in the upper of the hindlimb of a normal mouse. Combined US/PALI images are shown (pO_2 in mmHg color scale, ultrasound in 40dB gray scale). (a)-(c), tissue oxygen images reflecting tissue oxygen level under 21%, 80% and 10% oxygen in mixture nitrogen, as their imaging periods indicated (e). The values are given as the average ± standard deviation for all valid pixel values displayed. (d), photo of the mouse at imaging platform. The Arrow indicates the direction of laser illumination and the blue dashed box shows the area of imaging shown in (a)-(c). (e), simultaneous recording from the optical oxygen meter. Periods of gas mixture and PALI images are indicated.

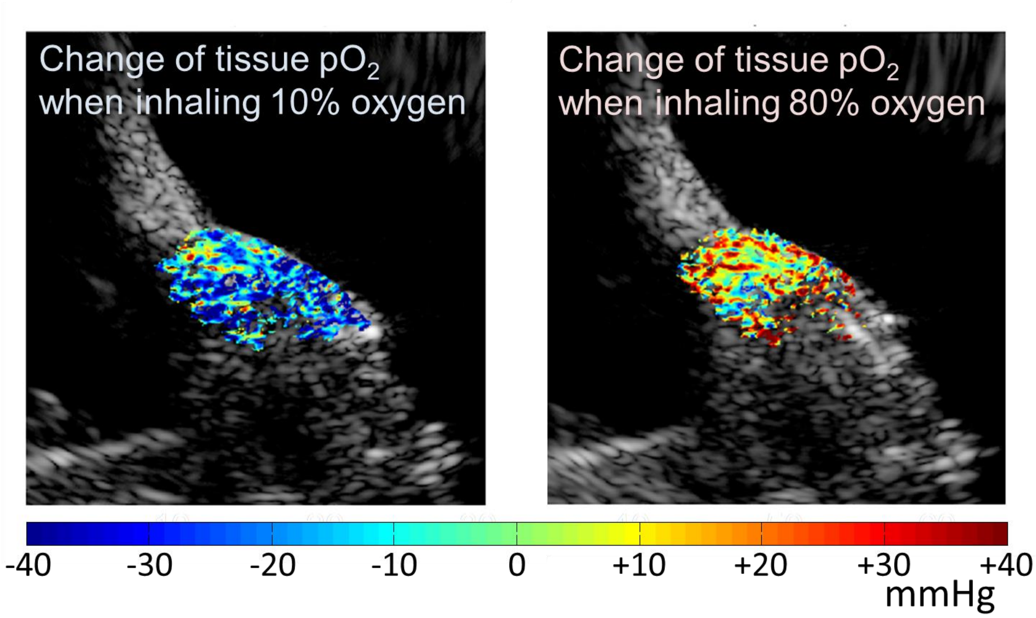

Figure 15 Pixel-by-pixel-based relative changes in tissue pO_2 due to modulated inhalation of low oxygen (10%) and high oxygen (80%) content respectively. Changes are calculated with respect to image acquired with normal air breathing.

3.3.2 Ischemia model

The imaging results of the acute ischemia model are shown in Fig 16. Even though the rubber band occlusion affected the extent of tissue ischemic hypoxia of the two animals differently (mostly due to differences in the tightness and location of the rubber band), the images clearly show differences in tissue oxygen between normal, ischemic, and reperfused states in Fig. 16. From the color scale of PALI images, the decrease in the tissue oxygen level under ischemia was captured. When the rubber band was removed, the recovery of blood flow increased the tissue oxygen level compared to the ischemic status.

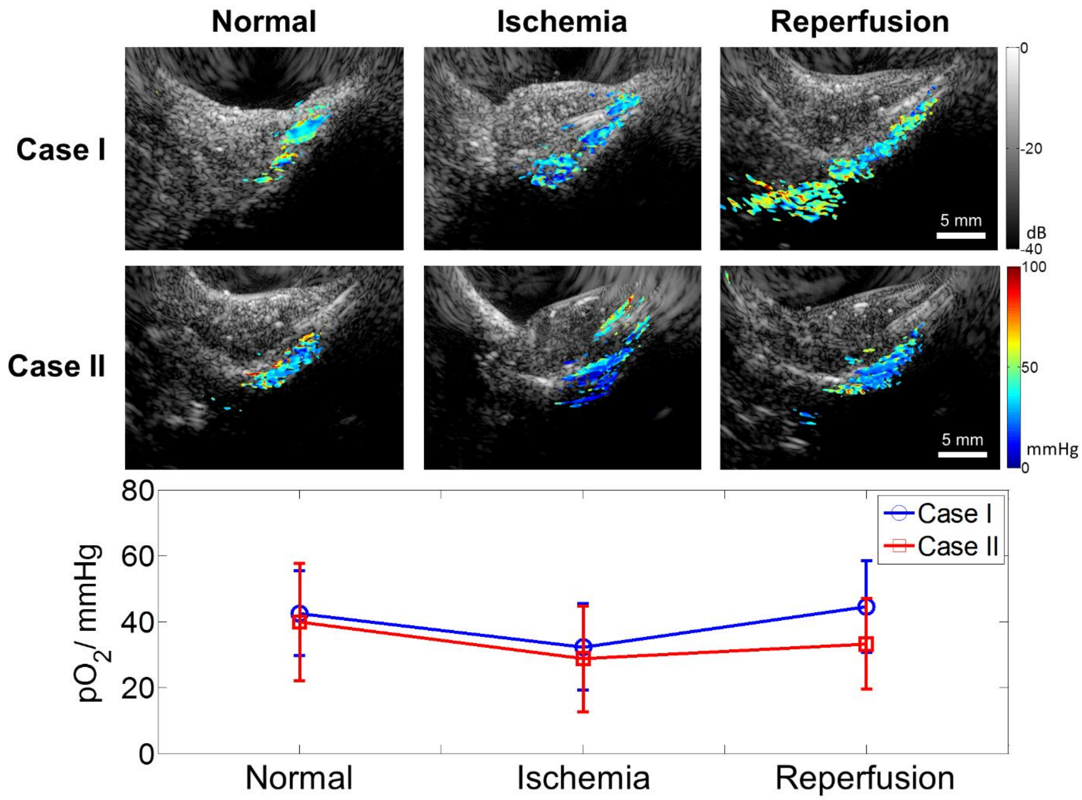

Figure 16 PALI tracking of pO_2 during blood flow restricting experiment in the upper part hindlimb of normal mice. Combined US/PALI images are shown before (column under normal), during flow restriction (ischemia), and immediately after releasing the restriction (reperfusion). Case I and II were experiments done on two mice. Statistics of the pixel values imaged are given by the average and error bars as standard deviation.

3.4 Conclusions and Discussions

We have demonstrated that PALI is able to reflect the change of oxygen levels, in a direct and non-invasive manner. Tissue oxygen changes were induced by two methods and were both captured by our imaging modality. A single point oxygen meter validated the imaging results. The changes of tissue oxygen obtained by PALI are highly correlated with the measurements obtained from the oxygen sensor. The increase of tissue oxygen due to high inhaled oxygen (80%) were both captured in our PALI images (average pO_2 changed from 52 mmHg to 63 mmHg) and oxygen sensor (from 52 $\pm$ 1 mmHg to 86 $\pm$ 3 mmHg). In additional, the drop of pO_2 values as a result of low oxygen (10%) breathing condition is observed from our PALI images (average of 32 mmHg) and confirmed by the direct measurement of oxygen sensor probe (drop to 24 $\pm$ 5 mmHg). The imaging system was able to visualize changes occurring within the time scale of a few minutes. This is valuable for identifying changes in pathophysiological conditions rapidly. The system was also able to capture the spatial distribution of pO_2 in a non-destructive manner compared to repeating single-point measurement. A multi-imaging modality (ultrasound, photoacoustic and photoacoustic lifetime) was integrated due to the nature of their common ultrasound acquisition module. The multimodal capacity enables structural, functional, and molecular imaging with a single setup.

Restricted by performance of our optical system, the current stage of our imaging modality has certain limitations. The laser system output (power at desired wavelength <100 mW) constrains the imaging area coverage, which has a surface area of about 2 cm^2 and a depth less than 1 cm. The variation of laser intensity and low repetition rate (10 Hz) both contribute to the relatively long acquisition time necessary for PA signal averaging in order to get reliable readings. Specifically, averaging of 50 measurements of acquired photoacoustic signal is used to improve the signal to noise ratio (SNR) by 17 dB. This amounts for a total acquisition time of less than 3 minutes for a single PALI image. The resolution is determined by the ultrasound transducer, which is used for photoacoustic signal detection and therefore resembles that of US imaging [36, 56]. In our system, the resolution is less than 0.5 mm by using a transducer with a bandwidth of 4-7 MHz. The pixel-to-pixel variations in pO_2 as depicted in PALI images is relatively high. In some cases sharp changes of up to 100 mmHg are observed within a distance of less than 1 mm. It is difficult to assert what part of these variations reflect the true oxygen heterogeneity in tissue and what part should be attributed to measurement error. Previous phantom experiments have shown that the measurement error is well below 20%[81]. Differences in pO_2 value between the commercial oxygen probe and PALI images are likely attributed to the fact that the point of probe measurement is not within the imaging area and to the heterogeneous nature of tissue oxygen. The tools and methods we presented here could be applied to further explore the dynamics of tissue oxygen. It would allow detailed study of spatial and temporal changes in tissue oxygen in response to therapeutic treatments or other modulations. Further work is needed to better quantify the in vivo accuracy of PALI oxygen imaging system.

PALI is very attractive for a wide range of clinical applications in which direct tissue oxygen assessment would improve therapy decision making and treatment planning. Examples include cancer treatments (radiotherapy and PDT) and treatments of diabetes-related ulcers. We anticipate that the ability to measure tissue oxygenation will enable physicians to better diagnose as well as to optimize treatment plans. A more comprehensive optimization of PALI is still required before its implementation into clinical applications could be developed. Substantial work is needed to further improve the imaging performance such as accuracy and speed. One of the methods to improve image acquisition speed is by adapting lasers with higher repetition rate and lower energy fluctuation, thus largely reduce the time for averaging signals. Another possible way is to reduce the time consumption of averaging is to have laser pulse energy monitored during the course of imaging, so that the intensity fluctuations of the lasers can be compensated. Other methods of light delivery, such as the use of minimally invasive, tissue-penetrating fiber diffusers, should be explored in order to extend the applicability of PALI into an even broader range of clinical applications.

3.5 Acknowledgments

The authors thank Ekaterina Morgounova for constructive discussions. The authors appreciate Kelsey Pflepsen’s close reading of the manuscript and support from Center of Writing, University of Minnesota. This work was sponsored by NIH R21 EB016763, R21 CA135027, NIH R01 CA183749 and IEM cancer animal core lab, University of Minnesota. Qi Shao was supported by Doctoral Dissertation Fellowship, University of Minnesota.

Chapter 4 Image-guided photodynamic therapy by photoacoustic lifetime imaging

This chapter is adapted from the following publications

"Noninvasive tumor oxygen imaging by photoacoustic lifetime imaging integrated with photodynamic therapy", Proc. of SPIE Vol. 8931, 89310H, 2014

Contributing Authors: Qi Shao, Merrill Biel and Shai Ashkenazi

"Tissue oxygen monitoring by photoacoustic lifetime imaging (PALI) and its application to image-guided photodynamic therapy (PDT)", Proc. of SPIE Vol. 9323, 932320, 2015

Contributing Authors: Qi Shao, Ekaterina Morgounova, Shai Ashkenazi

4.1 Introduction

4.1.1 PDT and tumor oxygen

Photodynamic therapy (PDT) is a treatment for neoplastic and abnormal tissues that uses a combination of photosensitizer together with light to induce necrosis and apoptosis of cells. Parameters such as type and concentration of photosensitizer, drug-light interval, light intensity and total light dose play a central role of effective and safe PDT.[96, 97] Another important factor for PDT is the oxygen status of the tumor.[98] Oxygen is a prerequisite for the photochemical reaction, and insufficient availability of oxygen reduces the efficiency of PDT. During the photochemical reaction, oxygen is consumed, and free radicals and highly toxic singlet oxygen, which cause cell death, are produced.[99] PDT can also cause extensive vascular damage, which leads to vasoconstriction and vessel occlusion. Two mechanisms act independently or cooperatively, result in the development of outcome-limiting hypoxia during PDT.[100] The heterogeneity of oxygen partial pressure (pO_2) in tumor has been well recognized.[23, 99, 101, 102] During PDT, the vascular shutdown process is likely heterogeneous, and the response within bulk tissue cannot be universally quantified by a single set of dosimetry conditions, because variations in vessel size, flow rate and distribution within a neovascularized tissue result in a heterogeneous response. The oxygen distribution with regards to the use of PDT for treating tumor tissue has also been studied. [23, 99, 102-107]

4.1.2 Tissue Oxygen Imaging

Most existing techniques apply indirect approach to assess oxygen contents by evaluating hypoxia related factors instead of direct measurement of oxygen. Non-invasive hypoxia-related imaging solutions had been developed for magnetic resonance imaging (MRI) and positron emission tomography (PET). F^{18}–FMISO PET is the most widely used hypoxia imaging modality. It relies on preferential accumulation of FMISO (fluoro-misonidazole) in hypoxic cells.[108] Since this process does not depend only on pO_2, but also on tissue type, it introduces inherent difficulties in standardizing the imaging protocol and interpreting the results. Other PET agents for hypoxia imaging are currently investigated. MRI is most commonly used for blood oxygenation imaging.[109] MRI T_2 relaxation time correlates with hemoglobin oxygenation. Assuming that hemoglobin bound oxygen is in equilibrium with tissue dissolved oxygen, it provides an indirect measure for tissue oxygenation. Several factors such as vasomodulation and distance from perfusion capillaries lead to deviations from equilibrium state thus limiting the reliability of the measurements.

Oxygen sensitive dyes have been developed for fluorescence oxygen imaging.[42] In the absence of oxygen these dyes exhibit long excited state lifetime which can be monitored by measuring time-dependent fluorescence. In the presence of oxygen, lifetime is shorter due to energy transfer to oxygen molecules. This effect is used for converting fluorescence lifetime information into 2D maps of oxygen level. It provides 2D surface imaging of tissue oxygen. The major limitation of this method is that there is no depth resolution so the image represents oxygen level at or near the surface.

The gold standard for measuring tissue oxygenation is galvanic electrode.[110] It is hardly used in clinical settings because it is invasive, provides only single point measurement at a time, and requires calibration.

4.1.3 Methylene Blue (MB) as a photosensitizer

MB is an important vital dye, widely used in different fields of medicine. The photophysics and photochemistry of MB has been well studied, and it has been well demonstrated that MB can be used in PDT to treat tumors. [93, 111-113] In this paper, we mainly discuss MB both as oxygen sensitive dye in our photoacoustic lifetime imaging (PALI) method and PDT for the following reasons: (1) MB is widely used in several other clinical applications. Its biocompatibility and safety are well studied and documented; (2) MB has been successfully studied for its use as an oxygen sensitive agent in PALI; (3) MB can be applied topically and intratumorally, preventing undesired skin photosensitivity following PDT treatments; (4) Efficacy of MB-PDT has been demonstrated in large-animal studies. MB is used as an example of serving both oxygen sensitive dye and photosensitizer.

4.1.4 Tissue oxygen imaging by photoacoustic lifetime imaging (PALI)

PALI has been demonstrated to be able to image tumor hypoxia in small animal model.[81] The basic principle of photoacoustic lifetime probing of oxygen is also well discussed.[35]

Upon light absorption, MB is efficiently (ISC=0.52) excited to a long-lived triplet state. The lifetime of the triplet state is 78 μs in O_2-free environment. In the presence of oxygen, the rate of triplet state relaxation back to ground state depends linearly on oxygen concentration. In fully aerated solution (pO_2=160 mmHg) the lifetime is 2 μs. PALI utilizes the fact that the optical absorption of MB at a second wavelength (810 nm) changes drastically from a negligible absorption of ground state to high absorption of the triplet state (due to triplet-triplet absorption). The absorption at 810 nm shows a transient behavior following excitation, reflecting the population of molecules at triplet state. Photoacoustic imaging can be used to acquire a snapshot of the transient absorption in an extended region of an MB stained object. Such a “snapshot” shows the distribution of optical absorption at a specific time delay after excitation (controlled by the time delay between excitation pulse and photoacoustic probing pulse). PALI consists of a series of excitation (660 nm) – probing (810 nm) pulse pairs and recording of photoacoustic generated wave by an ultrasound imaging array. The data acquired following each probing pulse is used to reconstruct a transient photoacoustic image corresponding to a specific delay. The series of photoacoustic images are processed in pixel-wise manner to extract the dynamics of transient absorption at each pixel location of the field of view. Pixel values at different time delays are fitted to an exponential decay function and the decay rate is extracted and converted to pO_2 value. The pO_2 values of all pixels are then presented as a pO_2 distribution map.

As mentioned above, the efficiency of triplet excitation is 52%. The rest of the absorbed energy is mostly converted to heat and therefore generates an undesired photoacoustic signal. It is undesired because it does not hold information on pO_2. The photoacoustic signals generated by the first pulse and the second pulse are in general overlapping. In our PALI signal processing we have separated these signals by recording a photoacoustic signal generated by excitation pulse only and then subtracting it from combined data signals.

Data validation criteria have been defined to reject unreliable measurements. These include a threshold signal amplitude (e.g. >0.25 of maximum) and coefficient of determination (e.g. R^2>0.8) of the exponential fit. Only pixels that pass both criteria are shown in the final pO_2 map.

4.1.5 The treatment-imaging modality

We are developing a treatment/imaging modality (PDT-PALI) that integrates PDT and a combined ultrasound/photoacoustic imaging system (Fig. 17). The system will provide real-time feedback of three essential parameters namely: tissue oxygen, light penetration in tumor location, and distribution of photosensitizer. The system will be designed for clinical treatments of cancer of the oral cavity. Tissue oxygen imaging will be performed by applying Photoacoustic Lifetime Imaging (PALI). This technology relies on photoacoustic probing of oxygen-dependent, excitation lifetime of Methylene Blue (MB) photosensitizer. Lifetime information can also be used to generate image showing the distribution of photosensitizer in tissue. The level and penetration depth of PDT illumination will be deduced from photoacoustic imaging at the same wavelength. All images will be combined with ultrasound B-mode images for anatomical reference.

4.2 Materials and methods

4.2.1 Combining MB-Mediated PDT with PALI

PALI and PDT are inter-related because both rely on spin-exchange interaction between an excited photosensitizer and molecular oxygen. In fact, PALI induces photosensitizer activation and therefore PDT action, however, the typical light dose associated with an acquisition of a single PALI frame is about 6 J/cm^2 (based on 10mJ/cm^2/pulse, 6 time delays, 100 averages), while the typical PDT light dose is about 120 - 600 J/cm^2. This similarity of the underlying molecular mechanism allows for using MB photosensitizer for both PALI and PDT.

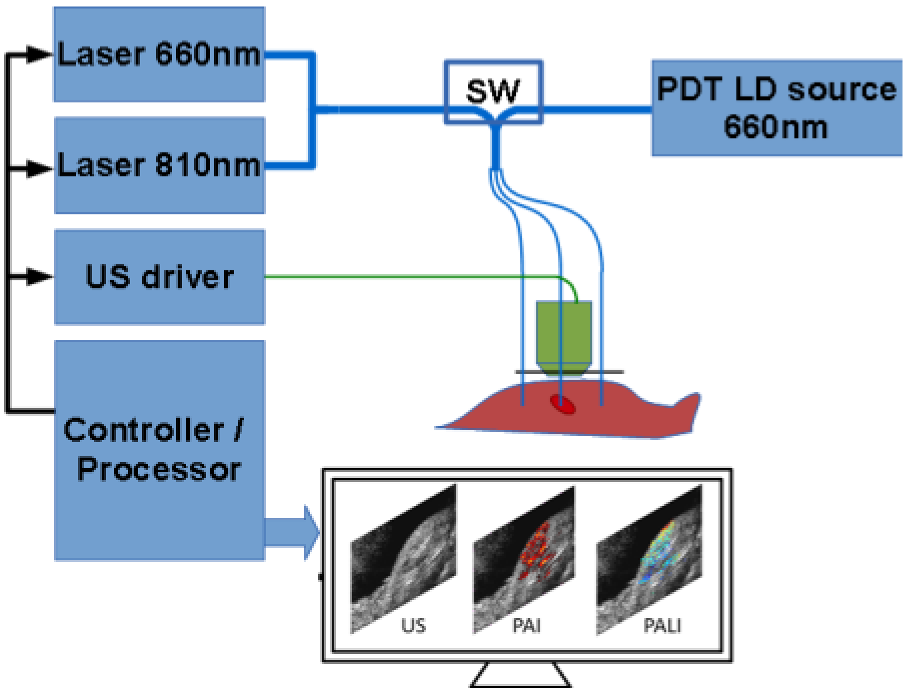

Figure 17 A combined PDT/PALI therapy/imaging system. A common fiber-optic bundle delivers light to the tissue using either non-invasive illumination or by a set of tissue-penetrating fiber diffusers. A 660 nm emitting laser-diode is used for PDT. Short pulse (6 ns) Nd:YAG lasers equipped with optical parametric oscillator are used for PALI excitation (660 nm) and photoacoustic probing (810 nm). Open development platform is used for ultrasound multi-channel data acquisition. 64-element US linear array is used for US, PAI, and PALI imaging operation. An FPGA module is used to synchronize laser firing and signal acquisition. A PC is used as a system controller, data processing and display.

4.2.2 Validation and optimization

The first steps of our proposed system focus on establishing solid indications that PALI measurements of pO_2 are reliable. In particular, we will verify its validity range with respect to changes in environmental parameters such as temperature and pH. Phantom experiments will be conducted to determine the precision of pO_2 measurement with respect to variations in dye concentration, depth of object, tissue pH level, and temperature.

Most of the validation and characterization assessments will be carried out on a phantom object. The phantom material would mimic acoustical and optical properties of tissue. The phantom will be immersed in a water tank to allow ultrasound coupling to the transducer. The temperature of the phantom will be controlled by connecting the water tank to an external temperature controller and water circulation system. The pH of the phantom will be controlled by using different pH buffered solutions for the MB solution. Fig. 18 shows a schematic diagram of the phantom system.

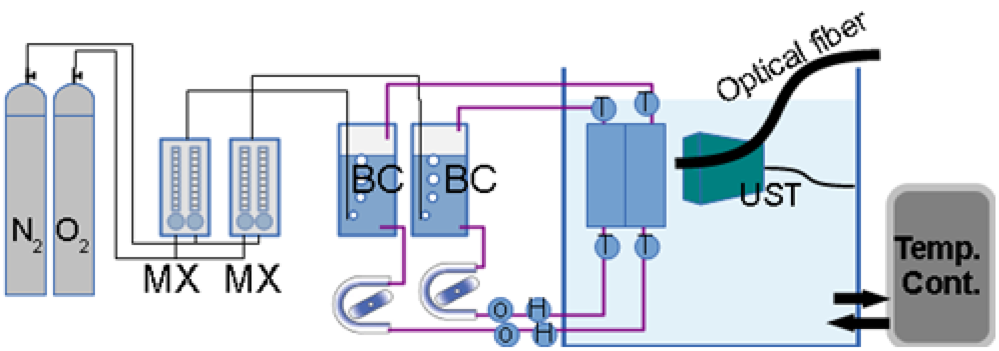

Figure 18 Phantom mimicking acoustic and optical tissue properties is immersed in water and contains two separate compartments. pO_2 in each compartment is individually controlled by bubbling different gas mixtures in bubbling cells (BC).Two peristaltic pumps maintain close flow of two MB solutions. In each close circulation temperature, pH and pO_2 are recorded. Water temperature is controlled. US transducer (UST) and optical fiber installed in water tank.

Phantom experiments are an effective tool for developing PALI, however, several aspects of the imaging method can only be optimized in the *in vivo* environment. In this phase, we will use small animal experiments to acquire information on optimal parameters and methodologies for applying PALI *in vivo*. In these experiments we focus on imaging parameters alone, in separation from further considerations related to PALI application to cancer tumors.

The objectives includes (1) the development a methodology for consistent and optimal dye injection, (2) the study of the extent of time following injection in which PALI provides valid data, (3) the study of effect of MB concentration on imaging depth, (4) correlation of PALI data and polarographic pO_2 needle electrode at one point in vivo.

4.2.3 Tissue oxygen distribution, imaging Mode: PALI-O_2

Upon light absorption, MB is efficiently (ISC=0.52) excited to a long-lived triplet state. In an O_2-free environment, the lifetime of the triplet state is 70 μs. In the presence of oxygen, the rate of the triplet state relaxation back to the ground state depends linearly on oxygen concentration. In fully aerated solution (pO_2=160 mmHg) the lifetime is 1.8 μs. [10] PALI utilizes the fact that the optical absorption of MB at a second wavelength (810 nm) changes drastically from a negligible absorption of ground state to high absorption of the triplet state (due to triplet-triplet absorption) [35]. The absorption at 810 nm shows a transient behavior following excitation, reflecting the population of molecules at triplet state. Photoacoustic imaging (PAI) [114, 115] can be used to acquire a snapshot of the transient absorption in an extended region of an MB stained object. Such a "snapshot" shows the distribution of optical absorption at a specific time delay after excitation (controlled by the time delay between excitation pulse and photoacoustic probing pulse). PALI consists of applying a series of pulse pairs (excitation pulse at 660 nm and probe pulse at 810 nm) and recording the photoacoustic generated wave by an ultrasound imaging array. The data, acquired following each probing pulse, are used to reconstruct a transient photoacoustic image corresponding to a specific delay. The series of photoacoustic images are processed in a pixel-wise manner to extract the dynamics of transient absorption at each pixel location of the field of view. Pixel values at different time delays are fitted to an exponential decay function and the decay rate is extracted and converted to pO_2 value. pO_2 values of all pixels are then presented as pO_2 distribution map. The rest of the absorbed energy is mostly converted to heat and therefore generates an additional photoacoustic signal. This signal does not hold information on pO_2. Photoacoustic signals generated by the first pulse and the second pulse are overlapping, in general. These signals are separated by recording a photoacoustic signal generated by excitation pulse only and then subtracting it from combined data signals. Data validation criteria have been defined to reject unreliable measurements. These include a threshold signal amplitude (>0.25 of maximum) and a coefficient of determination (R^2>0.8) of the exponential fit. Only pixels that pass both criteria are shown in the final pO_2 map.

4.2.4 Light penetration mapping, imaging Mode: PAI

The photoacoustic signal generated by the pump laser is used to reconstruct an image reflecting the absorption of light in tissue volume. This signal is generated by fast relaxation of singlet excitation of MB dye and by light absorption in other tissue components (mostly by hemoglobin and myoglobin). This mode of imaging will be used to provide an approximate assessment of light penetration in tissue.

4.2.5 Photosensitizer distribution, imaging Mode: PALI-AMP

In PALI image processing, both the exponential time and the amplitude of the exponential component are extracted. The amplitude is a measure of MB concentration because it reflects absorption of long lifetime (>1 μs) states (lifetime of all other tissue components is in the ns range). PALI amplitude maps are therefore useful for estimation of MB distribution in tissue.

4.2.6 Anatomical structure, ultrasound B-Mode

PALI imaging hardware is built using an OEM US imaging system which will be used to provide ultrasound B-mode images for aligning photoacoustic images with ultrasound-based anatomical images. All photoacoustic images (PALI-O_2, PALI-AMP, PAI) will be overlaid on ultrasonic gray-scale images.

4.2.7 Testing with large animal using PALI guided IT MB-PDT

Treatment efficacy is tightly connected to two key parameters: efficient excitation of the photosensitizer (MB), and abundance of oxygen to carry the excitation energy to the tissue. Both of these parameters can be mapped in real-time during the treatment by applying PALI imaging. The prime goal of is to figure out how the additional imaging information can be used to drive an improved effective delivery of PDT treatment.

4.3 Conclusion and discussions

The integrations of tissue oxygen imaging by PALI with PDT is intend to noninvasively optimize the effectiveness of intratumoral Methylene-Blue-mediated photodynamic therapy (IT MB-PDT) by measuring, and augmenting the pO_2 in the tumor environment, thereby improving the cancer treatment outcome and cure rate. PALI images can also provide a real-time assessment of light penetration to the treated site and guide individual optimization of PDT light dose

Implementation of PALI in PDT can also drive its application in guiding other cancer treatments that are affected by hypoxia such as radiotherapy and chemotherapy. Results obtained in this project can also establish the basis for developing PALI for other clinical applications such as oxygen mapping in diabetic ulcers.

The future work advances this technology further into clinical application by addressing several major aspects. The first is the shared use of optical fiber diffusers to enhance the uniformity and penetration of light for both PALI and PDT. Secondly, a unique ultrasound probe design is proposed to provide alignment of ultrasound field of view with the fiber diffusers and facilitate artifact-free imaging.

The successful outcome of our work should accurately determine the most efficacious MB drug light parameters and treatment methodology to be used and directly translated to an ultimate human clinical trial of IT MB-PDT of recurrent unresectable HNSCC. Particularly, the optimal use of PALI information in tailoring treatment parameters to improve PDT treatment in each individual patient will be established.

Chapter 5 Photoacoustic lifetime contrast for activatable probe

This chapter is adapted from the following publications

"Photoacoustic lifetime contrast between methylene blue monomers and self-quenched dimers as a model for dual-labeled activatable probes", Journal of Biomedical Optics 18(5), 056004 (May 2013)

Contributing Authors: Ekaterina Morgounova, Qi Shao, Benjamin Hackel, David Thomas, and Shai Ashkenazi

"In vitro characterization of a lifetime-based activatable photoacoustic probe" Proc. of SPIE Vol. 9323, 93232J, 2015

Contributing Authors: Ekaterina Morgounova, Sadie Johnson, Qi Shao, Benjamin Hackel, Michael Wilson and Shai Ashkenazi

5.1 Introduction

5.1.1 Photoacoustic molecular imaging

Photoacoustic molecular imaging is a nonionizing modality that provides high penetration depth and high spatial resolution information on the functional and metabolic status of diseases at greater depths than other optical imaging techniques.[116-118] Traditionally, photoacoustic imaging has been used with both endogenous contrast agents, such as hemoglobin and melanin, and exogenous contrast agents that exhibit higher optical absorption than normal tissue. Targeting molecular markers using exogenous smart probes can potentially reap valuable information about biological processes occurring at different stages of various diseases. As a result, photoacoustic molecular imaging could substantially aid the diagnosis of cancer by detecting subtle abnormalities at the molecular level well before the appearance of anatomical changes.

[119] This capability would also allow for personalized treatment planning and step-by-step evaluation of treatment efficacy.[117]

Activatable photoacoustic probes, in particular, provide a high imaging contrast by switching from a silent to a visible state upon cleavage by a target enzyme.[120, 121] Several such probes, based on a change in spectral absorption between the inactive and active states, have recently been developed to image protease activity in vitro[117, 118, 122] and in small animal models[123, 124]. However, the sensitivity of these probes is limited by heterogeneous background signal stemming from non-uniform light delivery and absorption to the volume of tissue.[125] To obtain a clinically relevant photoacoustic probe, background signal suppression needs to be improved.

5.1.2 Activatable Probes for Molecular Imaging

Activatable probes are a class of contrast agents that identify selective enzyme activity by switching from an inactive state to an active state upon interaction with a target enzyme.[121] Originally developed for fluorescence imaging, the probes contained a fluorophore-quencher pair coupled to a peptide linker bearing an enzymatic site. [120] Upon cleavage of the linker, the pair is separated and fluorescence is restored. This approach provides high contrast because of the low fluorescence background of the uncleaved, inactive form. Additionally, the fluorescence signal is further amplified due to the activation of multiple probes by a single enzyme. [126]

Activatable fluorescent probes have been successfully used in a wide range of small-animal imaging studies. However, the short penetration depth of light in tissue resulting from strong optical attenuation and scattering limits their translation to clinical applications and leads to poor spatial resolution beyond a few millimeters. [127] Photoacoustic imaging has emerged, in the last two decades, as an alternative optical modality offering significantly improved resolution (up to 0.02 mm) and penetration depth (up to 5 cm) in tissue imaging.[116] Its application has been demonstrated in clinical studies for breast cancer screening [128] and skin cancer diagnosis. [129]

Activatable photoacoustic probes have recently been proposed and studied by several groups. [117, 118] They rely on a change in the absorption spectrum upon activation to selectively detect the activated probe signal. This method requires multi-wavelength illumination to resolve the spectral contribution of each chromophore by linear fitting and also assumes that the spectral distribution of probes and tissue absorbers is known. In practice, non-uniform light distribution, due to wavelength-dependent attenuation, and heterogeneous optical properties of tissue may hamper accurate spectral identification and background signal suppression.

A new photoacoustic contrast mechanism based on switching the excited-state lifetime of the probe from short (<100 ns) to long (>2 μs) is proposed, as shown in Fig. 19. A pump-probe approach that eliminates the need for spectral deconvolution by measuring lifetime contrast using only two illumination wavelengths, is applied for the first time to selectively detect the signal from activated probes.

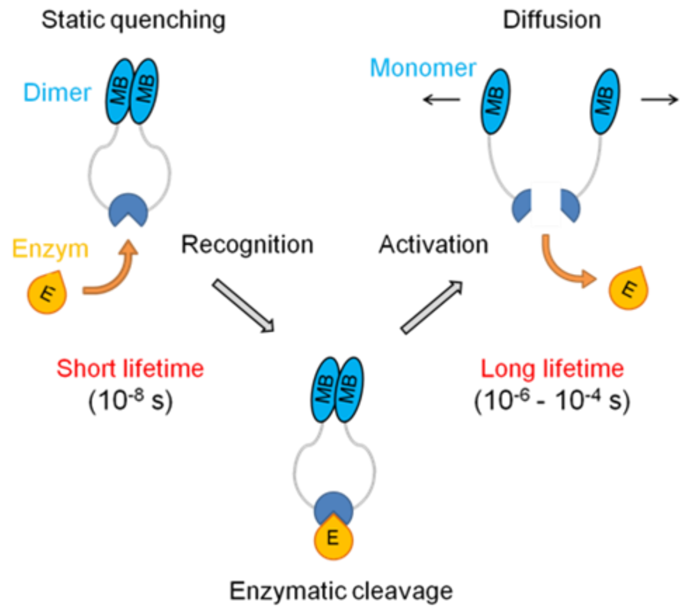

Figure 19 Schematic representation of proposed MB dual-labeled activatable probe containing a specific enzymatic site. The intact probe has a short lifetime of a few tens of nanoseconds. Enzymatic cleavage separates the chromophores thereby permitting them to recover their long excited-state lifetime (tens of microseconds).

5.1.3 Photoacoustic Lifetime Contrast Imaging (PLCI)

MB is a planar cationic dye of the phenothiazine family that is commonly used, or under study, in several therapeutic and diagnostic applications. [113, 130] Both orally and intravenously administered MB is excreted by the kidneys either unchanged or reduced to leucomethylene blue by the enzyme methemoglobin reductase present in red blood cells. [131, 132]

Following optical absorption, the ground state molecule (S_0) is excited into a singlet state (S_1), and then undergoes intersystem crossing (ISC) to a metastable triplet state (T_1) with high quantum yield (Φ_{ISC} =0.50) [133]. The excited triplet state lifetime is typically tens of microseconds in an oxygen-free environment because of the spin-forbidden nature of the $T_1 - S_0$ transition. Collisional quenching by oxygen, however, decreases this lifetime to approximately 2 μs in aerated solutions at atmospheric pressure. [35]

Molecular association between monomers occurs spontaneously in water due to a combination of hydrophobic interactions, hydrogen bonding, and Van der Waals forces.[134, 135] The coupling between monomers results in a splitting of the singlet excited state into two states, of lower and upper energies, which manifests by a splitting of the absorption band of the monomer, as shown in Fig. 20. If a dimer is excited to the upper state S_1, it undergoes very fast (10^{-12} s) internal conversion to the lower state S_1' and, because transitions from S_1' to S_0 are forbidden, ISC is enhanced. If the coupling between monomers is strong, electron transfer is expected to occur between the pair which results in triplet lifetime quenching and formation of transient radical ion pairs.

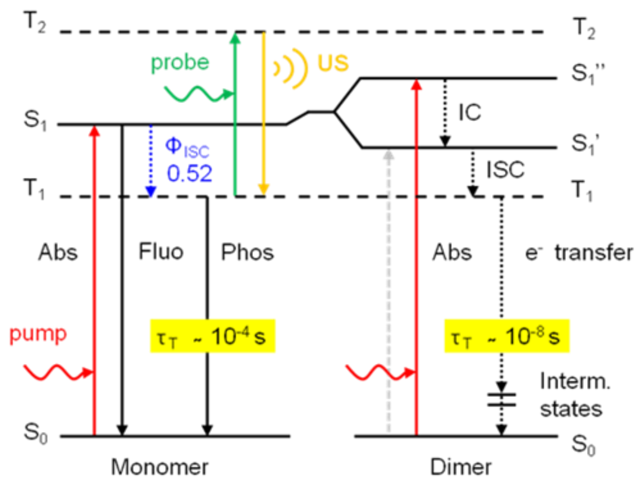

Figure 20 Energy diagram of MB monomer and dimer. Plain lines represent radiative transitions. Small downward dashed lines represent non-radiative processes. The energy of the T_1:T_2 absorption is converted into a photoacoustic relaxation signal. The double bar indicates a discontinuity in the transition diagram:

the dimer triplet undergoes electron transfer (~40 ns) which leads to the formation of oppositely charged radicals that relax to the ground state via charge recombination (~10^{-6} to 10^{-4} s). S_0: ground state, S_1: singlet excited state, T_1: primary triplet excited state, T_2: secondary triplet excited state, S_1' and S_1'': split exciton states, ISC: intersystem crossing, IC: internal conversion.

PLCI is a pump-probe approach that consists of applying an initial laser pulse (pump) to excite the dye to the T_1 state and a secondary pulse (probe) to excite T_1 to a T_2 state resulting in ultrasound waves generated during the $T_2 \rightarrow T_1$ photoacoustic relaxation. With this technique, the amplitude of the measured photoacoustic signal corresponds to the sum of the lifetime-dependent photoacoustic relaxation, a quantity proportional to the optical absorption of the T_1 state, and the lifetime- independent background photoacoustic signal due to the excitation of the background environment by the probe pulse. The photoacoustic contrast by transient absorption is shown in Fig. 21.

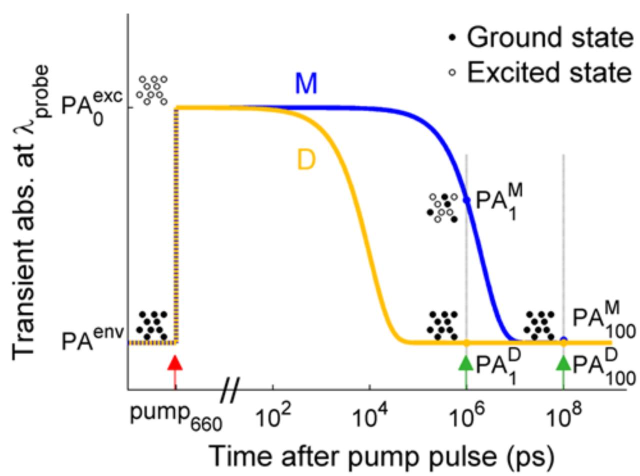

Figure 21 Normalized transient photoacoustic signal for MB monomer (τ=4 μs), dimer (τ=40 ns), and hemoglobin (τ =0.22 ns).

5.1.4 MMP-2 specific activatable probe

The probe was designed to be specific to matrix metalloproteinase 2 (MMP-2), a well-characterized collagenase involved in several stages of the metastatic cascade [136-138], and typically overexpressed in several types of tumors. [139, 140] We chose the hexapeptide Pro-Leu-Gly-Leu-Ala-Gly (PLGLAG) for a cleavage site because it is a well-established MMP-2 specific recognition sequence [141], and because it promotes the coupling between MB molecules by introducing an angle in thepeptide backbone due to the cyclic nature and conformational rigidity of its N-terminal proline. [142]

In the native state, the probe will dimerize due to a combination of electrostatic interactions and a strong indirect covalent bond, and exhibit a short photoacoustic lifetime. In the presence of MMP-2, the two side chains will separate and the chromophores will recover their long excited-state lifetime that can be imaged using a technique called photoacoustic lifetime imaging (PALI). In addition, the lifetime of MB monomers is at least 3 orders of magnitude greater than that of the main tissue absorbers (such as hemoglobin, melanin and albumin). It is therefore possible to selectively image the monomer signal while also effectively suppressing the background tissue signal by setting a threshold on the lifetime.

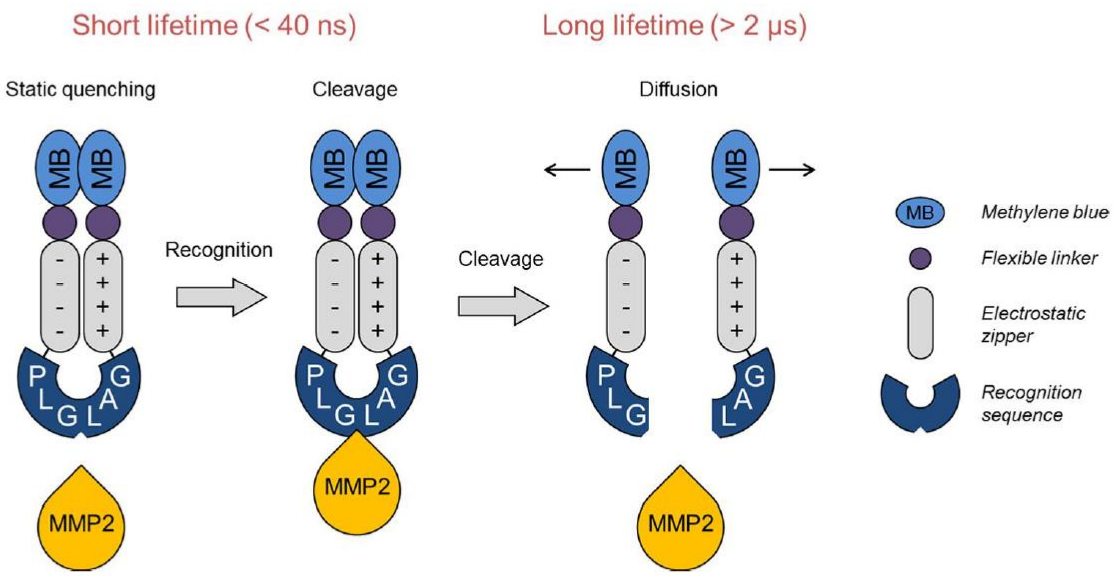

Figure 22 The photoacoustic probe design is composed of a MMP-2 recognition sequence PLGLAG, an electrostatic zipper comprising poly-arginine and poly-glutamate domains, a flexible linker and a pair of methylene blue chromophores. The intact probe has a short lifetime of a few nanoseconds due to static quenching. Upon cleavage of the recognition sequence, the peptide unzips causing the MB-bearing side chains to diffuse away and recover their long lifetime (several microseconds).

5.2 Materials and methods

5.2.1 Materials

Methylene Blue hydrate (purum ≥ 97%), and SDS (≥ 99.0%) were acquired from Sigma-Aldrich (St. Louis, Missouri) and sodium sulfate anhydrous (ACS) was acquired from Mallinckrodt Chemicals (Phillipsburg, New Jersey). All chemicals were dissolved without further purification in distilled water. Experiments were performed at 22 +/- 1 ℃, and the pH of the solutions was measured to be within 6.7 +/- 0.9. Changes in temperature and pH level, in these ranges, do not have a significant effect on MB dimerization.

5.2.2 Photoacoustic lifetime contrast imaging experimental setup

A PLCI experimental setup was used to probe the photoacoustic signal of plastic tubes filled with dye, or SDS/dye solutions as illustrated in Fig. 23. Two tunable Nd:YAG pulsed-laser systems (Surelite I-10, Continuum and Quantel, Brilliant both having f =10 Hz, pulse width = 5 ns), each coupled to an OPO (Opotek MagicPrism, Califonia), delivered the pump and probe pulses (6 and 8 mJ, respectively). The output of both OPO systems was coupled to a bifurcated light guide (MWG-1000S-SD) to ensure uniform illumination of the plastic tubes. The tubes were immersed in a water tank and a focused ultrasound transducer (Panametrics, V382, 3.5 MHz for salt experiment or V311, 10 MHz for SDS experiment) aligned with the incident laser beams detected the photoacoustic signals generated in the samples. Laser firing and ultrasound acquisition were synchronized by a field-programmable gate array (FPGA, KNJN, FX2 Saxo). Signals were amplified by 50 dB (Panametrics, 5072PR), recorded by a digital oscilloscope (Lecroy Wavejet 354), and transferred to a computer for processing. B-mode images were acquired by scanning the tubes, perpendicular to their long axis, using a motorized actuator (T-LA28A, Zaber) mounted on a translation stage. In order to maximize contrast, the wavelengths of both beams were independently tuned near the maximum of absorption for the monomer and triplet species, and within the range of maximal output energy for the OPOs.

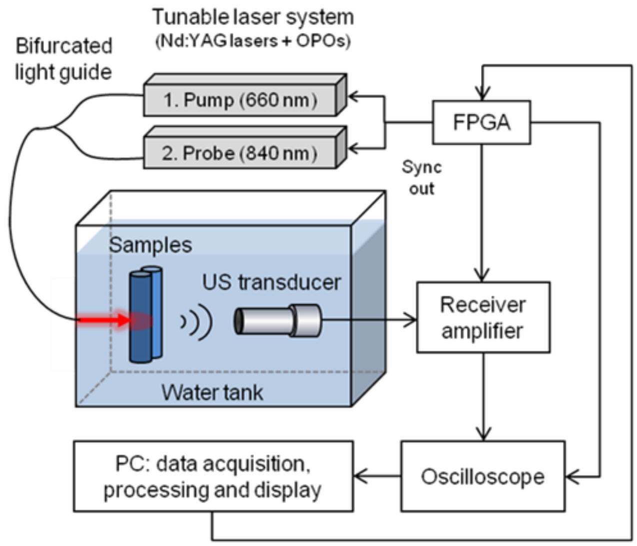

Figure 23 PLCI experimental setup. Pulsed outputs of the excitation laser (660 nm) and photoacoustic laser (840 nm) were combined with a bifurcated light guide and illuminate the target. The time delay between the excitation and probe pulses was controlled by an electronic synchronization circuit. The solutions were placed in two plastic tubes and scanned horizontally. The generated acoustic waves were detected by a focused ultrasound transducer. Sync out: synchronization output.

5.2.3 Peptide synthesis and conjugation

Methylene blue-N-hydroxysuccinimide ester dye (MB-NHS) was purchased from ATTO-TEC (Siegen, Germany), suspended in dry DMSO, and stored at -20 ℃. Peptides were purchased from UnitedPeptide (Herndon, VA), and suspended in 20 parts v/v PBS and 1 part v/v 0.2 M sodium bicarbonate (pH 9) for a final buffer pH of 8.3. To label each peptide terminus with MB, a 3-6 molar excess of MB-NHS was added to each peptide and allowed to incubate for more than 24 hours at room temperature. The reaction was then purified via reverse-phase HPLC and peaks containing dual-labeled peptides (MB_2-P) were collected. Peak purity was verified via mass spectrometry (Applied Biosystems-

Sciex 5800 MALDI-TOF/TOF, Framingham, MA). MB-Kz(e)$_n$[Ahx]PLGLAG(r)$_m$zK-MB products were then lyophilized, resuspended in d$H_2$0 and stored at 4 ℃.

5.2.4 MMP-2 activation photoacoustic experimental setup

The PLCI setup used to measure the triplet excited-state lifetime of the probes is illustrated in Fig. 24. A 3D printed photoacoustic chamber ensures the optimal and repeatable alignment of a sample-filled plastic tube with a randomized bifurcated light guide (Moritex, MWG-1000S-SD), and a focused ultrasound transducer (Panametrics, V311, 10 MHz). The pump and probe light pulses were delivered by two OPO systems (MagicPRISM, Opotek), each pumped by a Nd:YAG laser (Surelite I-10, Continuum and Quantel, Brilliant, f = 10 Hz, pulse width = 5 ns). The optical energies after the lightguide were 10 and 5 mJ for the pump (660 nm) and probe (830 nm), respectively. Finally, laser firing and ultrasound acquisition, as well as the delay between the two pulses, were controlled by a field-programmable gate array (FPGA, KNJN, FX2 Saxo). Photoacoustic measurements were recorded by a digital oscilloscope (Lecroy, LC584) and processed with MATLAB.

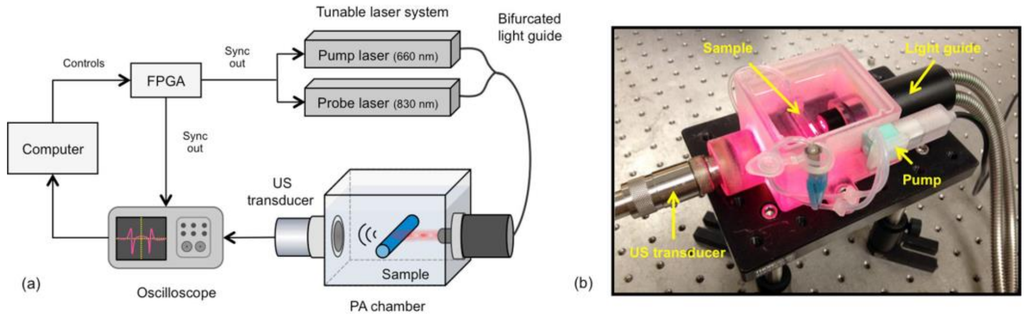

Figure 24 Photoacoustic experimental setup for MMP-2 activated probe. (a) Photoacoustic experimental setup. Pump (660 nm) and probe (830 nm) pulsed laser light are combined in a bifurcated light guide to excite a sample-filled plastic tube immersed in a 3D printed photoacoustic chamber filled with water. The generated photoacoustic signal is detected by a focused ultrasound transducer (10 MHz), amplified and displayed on an oscilloscope. The time delay between the pump and probe pulses is controlled by an FPGA. (b) Photoacoustic chamber during laser firing. A peristaltic pump was used to bring the solution in alignment with the light guide and the ultrasound transducer. Sync out: synchronization output.

5.3 Results and discussions

5.3.1 PLCI Imaging Between MB Monomers and Dimers in SDS

Two plastic tubes, respectively containing 200 μM MB +4 mM SDS (top) and 200 μM MB (bottom) solutions, were scanned by the PLCI system [Fig. 25(a)]. We estimated that the samples contained 5 and 110 μM monomer concentrations, respectively.

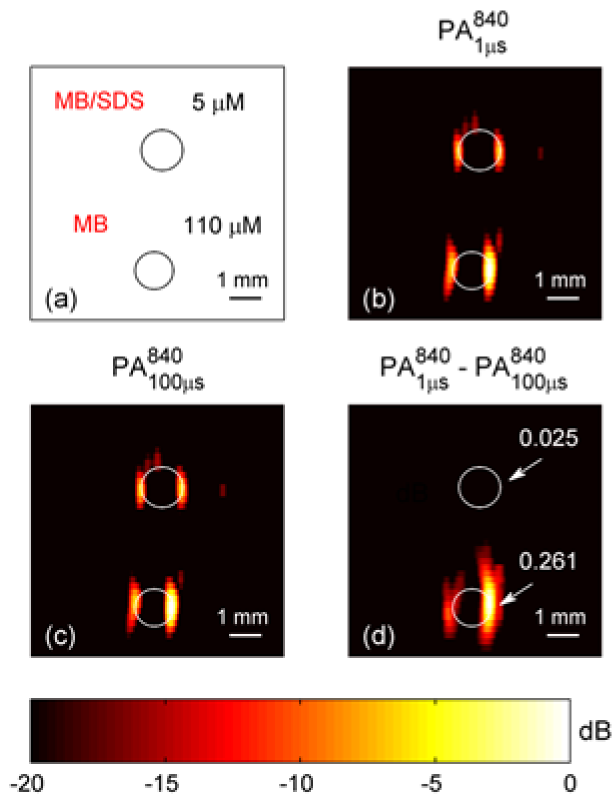

Figure 25 Photoacoustic lifetime contrast imaging is demonstrated by MB dimer and monomer. (a) Schematic representation of the position and size of the plastic tubes. Monomer concentrations are given in each case. (b) Photoacoustic amplitude image at 840 nm recorded 1 μs after the excitation pulse shows the signal generated at the plastic wall–solution interfaces. (b) Photoacoustic amplitude image at 840 nm recorded 100 μs after the excitation pulse. (d) Difference between photoacoustic amplitude images at 1 and 100 μs. There is a 21.5 dB suppression of the background signal due to the short lifetime of MB dimers. The numbers represent the value of the contrast parameter CPLCI at the front wall of the tubes.

The samples were probed by a 10 MHz ultrasound transducer scanned perpendicularly to the tubes axis in a range of 8 mm and with step size 0.2 mm. The signals were averaged over 32 measurements to compensate for pulse-by-pulse energy variations. The scanning time was relatively short (40 minutes) so that a majority of dimers (90%) remained stable during the experiment. At each step we calculated the photoacoustic probe signal by subtracting the signal generated without probe (excitation only) to the signal recorded with both beams (excitation + probe): $PA_{840\ (t = \tau)} = (PA_{660+840} - PA_{660})_{t = \tau}$. The difference between the signal at 1 µs and the signal at 100 µs was computed to remove the contribution from the static background environment. The signals were processed with a Wiener filter followed by a low-pass filter (Buttersworth, 6^{th} order, cut off frequency at 6 MHz) and the envelope was detected by the Hilbert transform method. $PA_{840\ (t = 1\ \mu s)}$, $PA_{840\ (t = 100\ \mu s)}$ images and their difference were displayed on 20 dB scale (Fig. 25 (b), (c) and (d)) and have a resolution of 0.32 mm. The circles correspond to the location and size of the plastic tubes.

5.3.2 Self-quenching efficiency

Photoacoustic probing of a 50 µM GE4R5G peptide solution was performed before and after 30 minutes activation by 2 ng/µL MMP-2 at 37 ℃. Fig. 26 (a) represents the transient photoacoustic signal of both forms of the probe for increasing pump-probe delay times (100 ns, 1 µs, and 2 µs). It was calculated by subtracting the signal generated with the pump (excitation only) and the signal generated with the probe (probing only) to the signal recorded with both beams (excitation + probing) to obtain: $PA_{transient} = PA_{660+830} - PA_{660} - PA_{830}$. As ground state MB molecules do not absorb at 830 nm, the signal obtained with the probe only (PA_{830}) corresponds to the photoacoustic energy generated by the static background - in this example, the plastic walls of the tubes. Before acquisition, the signals were averaged over 64 measurements to compensate for pulse-by-pulse energy variations. Finally, the transient signal was processed with a Wiener filter to reduce the noise. The front and back dye/plastic interfaces are visible at x = 2.8 mm and x = 4.2 mm respectively.

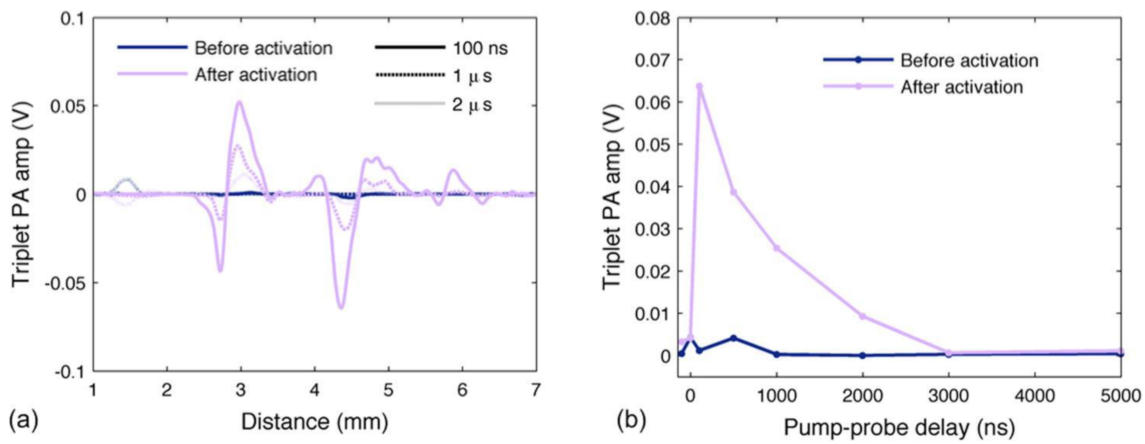

Figure 26 Triplet PA amplitude changes with activation of probe by MMP-2 due to the lifetime contrast. (a) Transient photoacoustic amplitude signal of a solution of GE4R5G probe at 50 μM before and after 30 minutes incubation with MMP-2 enzyme (2 ng/μL) at three different pump-probe delay times (100 ns, 1 μs and 2 μs). (b) Transient photoacoustic lifetime signal as a function of pump-probe delay time of the same solutions.

The corresponding lifetime signal (Fig. 26 (b)) was obtained by plotting the maximum of the envelope of the signal averaged over the two dye/plastic interfaces for each pump-probe time delay. One can see that the activated probe displays a 50-fold increase in transient photoacoustic amplitude following excitation whereas no increase, and therefore no lifetime signal, can be observed for the inactive probe. We calculated a lifetime of 0.92 μs by fitting an exponential curve for the active probe signal with a R^2 of 0.995. We conclude that the uncleaved probe is efficiently quenched whereas the active probe retains the transient PA signal arising from MB excited-state triplets.

5.4 Conclusions

Here, we present a new contrast mechanism for photoacoustic imaging based on the difference in excited-state lifetime between monomer and dimer forms of a chromophore. A model system makes use of a surfactant (SDS) to induce MB dimerization. The PLCI imaging experiment reveals a contrast of more than 20 dB between two samples of equal MB concentration, one containing free MB solution and the other containing SDS-MB for maximal MB dimerization.

Activatable smart probes have been developed as research tools for studying protein conformational dynamics, [143, 144] for detecting nucleic acid hybridization[120, 145], and for sensing enzymatic activity of disease biomarkers[124, 141, 146, 147]. Based on the previous measurements, we propose a new mechanism for an activatable photoacoustic probe. In its simplest form, the probe relies on a custom-made peptide linker bearing a specific enzymatic site and confining two MB molecules to a dimer configuration. This configuration results in an intact, quenched probe of short lifetime. Reaction with endogenous enzymes cleaves the linker and separates the probe into MB monomers. The PLCI system would be used to selectively detect the long-lifetime signal from activated probes (monomers) which would provide a map of both enzyme location and activity. The lack of other long-lifetime molecules in the body empowers the sensitivity of this approach.

It is our hope that our work on activatable probes for photoacoustic lifetime imaging will lay the groundwork for continuing research in the field of clinical molecular imaging thanks to the high resolution, high penetration depth and high sensitivity of our system. Ultimately, this technique could be used as an early-stage diagnosis tool, as well as for personalized treatment planning and continuous monitoring of the treatment efficacy.

5.5 Acknowledgments

The authors are grateful to C. Sheaff for his assistance in reading the manuscript. This project was supported by NIH grant 1R21CA135027-01A1.

Bibliography

[1] S. Ashkenazi, S. W. Huang, T. Horvath *et al.*, "Photoacoustic probing of fluorophore excited state lifetime with application to oxygen sensing," Journal of Biomedical Optics, 13(3), (2008).

[2] D. B. Papkovsky, G. V. Ponomarev, W. Trettnak *et al.*, "PHOSPHORESCENT COMPLEXES OF PORPHYRIN KETONES - OPTICAL-PROPERTIES AND APPLICATION TO OXYGEN SENSING," Analytical Chemistry, 67(22), 4112-4117 (1995).

[3] Y. F. Cao, Y. E. L. Koo, and R. Kopelman, "Poly(decyl methacrylate)-based fluorescent PEBBLE swarm nanosensors for measuring dissolved oxygen in biosamples," Analyst, 129(8), 745-750 (2004).

[4] D. Sud, W. Zhong, D. G. Beer *et al.*, "Time-resolved optical imaging provides a molecular snapshot of altered metabolic function in living human cancer cell models," Optics Express, 14(10), 4412-4426 (2006).

[5] K. Orth, G. Beck, F. Genze *et al.*, "Methylene blue mediated photodynamic therapy in experimental colorectal tumors in mice," Journal of Photochemistry and Photobiology B: Biology, 57(2), 186-192 (2000).

[6] I. Fukui, M. Yokokawa, G. Mitani *et al.*, "In vivo staining test with methylene blue for bladder cancer," J Urol, 130(2), 252-5 (1983).

[7] E. M. Tuite, and J. M. Kelly, "Photochemical interactions of methylene blue and analogues with DNA and other biological substrates," J Photochem Photobiol B, 21(2-3), 103-24 (1993).

[8] J. Clifton, 2nd, and J. B. Leikin, "Methylene blue," American journal of therapeutics, 10(4), (2003).

[9] G. C. Buehring, and H. M. Jensen, "Lack of Toxicity of Methylene Blue Chloride to Supravitally Stained Human Mammary Tissues," Cancer Research, 43(12 Part 1), 6039-6044 (1983).

[10] M. Gonzalez-Bejar, P. Montes-Navajas, H. Garcia *et al.*, "Methylene Blue Encapsulation in Cucurbit 7 uril: Laser Flash Photolysis and Near-IR Luminescence Studies of the Interaction with Oxygen," Langmuir, 25(18), 10490-10494 (2009).

[11] M. Xu, and L. V. Wang, "Photoacoustic imaging in biomedicine," Review of scientific instruments, 77(4), 041101 (2006).

[12] S. Ashkenazi, T. Horvath, Y.-E. L. Koo *et al.*, "Photoacoustic probing of fluorophore excited state lifetime with application to oxygen sensing," Journal of Biomedical Optics, 13(3), 034023-034023 (2008).

[13] [https://www.utwente.nl/tnw/bmpi/research/photoacoustic-imaging/].

[14] M. E. Hardee, M. W. Dewhirst, N. Agarwal *et al.*, "Novel imaging provides new insights into mechanisms of oxygen transport in tumors," Curr Mol Med, 9(4), 435-41 (2009).

[15] O. Thews, D. K. Kelleher, M. Hummel *et al.*, “Can tumor oxygenation be improved by reducing cellular oxygen consumption,” Adv Exp Med Biol, 471, 525-32 (1999).
[16] P. Okunieff, M. Hoeckel, E. P. Dunphy *et al.*, “OXYGEN-TENSION DISTRIBUTIONS ARE SUFFICIENT TO EXPLAIN THE LOCAL RESPONSE OF HUMAN BREAST-TUMORS TREATED WITH RADIATION ALONE,” International Journal of Radiation Oncology Biology Physics, 26(4), 631-636 (1993).
[17] M. Hockel, C. Knoop, K. Schlenger *et al.*, “INTRATUMORAL PO2 PREDICTS SURVIVAL IN ADVANCED CANCER OF THE UTERINE CERVIX,” Radiotherapy and Oncology, 26(1), 45-50 (1993).
[18] A. Bratasz, R. P. Pandian, Y. Deng *et al.*, “In vivo imaging of changes in tumor oxygenation during growth and after treatment,” Magnetic Resonance in Medicine, 57(5), 950-959 (2007).
[19] J. M. Brown, “The Hypoxic Cell: A Target for Selective Cancer Therapy—Eighteenth Bruce F. Cain Memorial Award Lecture,” Cancer Research, 59(23), 5863-5870 (1999).
[20] J. G. Rajendran, and K. A. Krohn, “Imaging hypoxia and angiogenesis in tumors,” Radiologic Clinics of North America, 43(1), 169-+ (2005).
[21] C. Menon, and D. L. Fraker, “Tumor oxygenation status as a prognostic marker,” Cancer Letters, 221(2), 225-235 (2005).
[22] S. M. Evans, and C. J. Koch, “Prognostic significance of tumor oxygenation in humans,” Cancer Letters, 195(1), 1-16 (2003).
[23] P. Vaupel, K. Schlenger, C. Knoop *et al.*, “Oxygenation of Human Tumors: Evaluation of Tissue Oxygen Distribution in Breast Cancers by Computerized O2 Tension Measurements,” Cancer Research, 51(12), 3316-3322 (1991).
[24] D. S. Vikram, J. L. Zweier, and P. Kuppusamy, “Methods for noninvasive imaging of tissue hypoxia,” Antioxidants & Redox Signaling, 9(10), 1745-1756 (2007).
[25] J. C. Hebden, A. Gibson, R. M. Yusof *et al.*, “Three-dimensional optical tomography of the premature infant brain,” Physics in Medicine and Biology, 47(23), 4155-4166 (2002).
[26] D. F. Wilson, S. A. Vinogradov, P. Grosul *et al.*, “Oxygen distribution and vascular injury in the mouse eye measured by phosphorescence-lifetime imaging,” Applied Optics, 44(25), 5239-5248 (2005).
[27] B. J. Krause, R. Beck, M. Souvatzoglou *et al.*, “PET and PET/CT studies of tumor tissue oxygenation,” Quarterly Journal of Nuclear Medicine and Molecular Imaging, 50(1), 28-43 (2006).
[28] R. C. Urtasun, M. B. Paliament, A. J. McEwan *et al.*, “Measurement of hypoxia in human tumours by non-invasive SPECT imaging of iodoazomycin arabinoside,” British Journal of Cancer, 74, S209-S212 (1996).

[29] J. L. Tatum, G. J. Kelloff, R. J. Gillies *et al.*, "Hypoxia: importance in tumor biology, noninvasive measurement by imaging, and value of its measurement in the management of cancer therapy," International journal of radiation biology, 82(10), 699-757 (2006).
[30] M. Stubbs, "Application of magnetic resonance techniques for imaging tumour physiology," Acta Oncologica, 38(7), 845-853 (1999).
[31] J. X. Yu, V. D. Kodibagkar, W. N. Cui *et al.*, "F-19: A versatile reporter for non-invasive physiology and pharmacology using magnetic resonance," Current Medicinal Chemistry, 12(7), 819-848 (2005).
[32] M. Elas, B. B. Williams, A. Parasca *et al.*, "Quantitative tumor oxymetric images from 4D electron paramagnetic resonance imaging (EPRI): Methodology and comparison with blood oxygen level-dependent (BOLD) MRI," Magnetic Resonance in Medicine, 49(4), 682-691 (2003).
[33] T. Liebgott, H. H. Li, Y. M. Deng *et al.*, "Proton electron double resonance imaging (PEDRI) of the isolated beating rat heart," Magnetic Resonance in Medicine, 50(2), 391-399 (2003).
[34] Q. Chen, H. Chen, and F. W. Hetzel, "Tumor oxygenation changes post-photodynamic therapy," Photochem Photobiol, 63(1), 128-31 (1996).
[35] S. Ashkenazi, "Photoacoustic lifetime imaging of dissolved oxygen using methylene blue," Journal of Biomedical Optics, 15(4), 040501-040501 (2010).
[36] A. Buehler, X. L. Dean-Ben, J. Claussen *et al.*, "Three-dimensional optoacoustic tomography at video rate," Optics express, 20(20), 22712-22719 (2012).
[37] S. A. Ermilov, M. P. Fronheiser, H.-P. Brecht *et al.*, "Development of laser optoacoustic and ultrasonic imaging system for breast cancer utilizing handheld array probes," 717703-717703 (2009).
[38] K. H. Song, and L. V. Wang, "Deep reflection-mode photoacoustic imaging of biological tissue," Journal of Biomedical Optics, 12(6), 060503 (2007).
[39] G. Ku, and L. V. Wang, "Deeply penetrating photoacoustic tomography in biological tissues enhanced with an optical contrast agent," Opt Lett, 30(5), 507-9 (2005).
[40] J. Clifton, 2nd, and J. B. Leikin, "Methylene blue," Am J Ther, 10(4), 289-91 (2003).
[41] A. Ray, J. R. Rajian, Y.-E. K. Lee *et al.*, "Lifetime-based photoacoustic oxygen sensing in vivo," Journal of Biomedical Optics, 17(5), 057004-057004 (2012).
[42] I. Dunphy, S. A. Vinogradov, and D. F. Wilson, "Oxyphor R2 and G2: phosphors for measuring oxygen by oxygen-dependent quenching of phosphorescence," Analytical biochemistry, 310(2), 191-198 (2002).
[43] L. S. Ziemer, W. M. F. Lee, S. A. Vinogradov *et al.*, "Oxygen distribution in murine tumors: characterization using oxygen-dependent quenching of phosphorescence," Journal of Applied Physiology, 98(4), (2005).

[44] A. Y. Lebedev, A. V. Cheprakov, S. Sakadzic *et al.*, "Dendritic Phosphorescent Probes for Oxygen Imaging in Biological Systems," Acs Applied Materials & Interfaces, 1(6), (2009).
[45] I. American National Standards, and A. Laser Institute of, [American National Standard for Safe Use of Lasers: ANSI Z136.1-2000] The Institute, (2000).
[46] J. A. Jensen, S. I. Nikolov, K. L. Gammelmark *et al.*, [Synthetic aperture ultrasound imaging], Netherlands(2006).
[47] I. Trots, A. Nowicki, and M. Lewandowski, "Synthetic Transmit Aperture in Ultrasound Imaging," Archives of Acoustics, 34(4), 685-695 (2009).
[48] M. H. Pedersen, K. L. Gammelmark, and J. A. Jensen, "In-vivo evaluation of convex array synthetic aperture imaging," Ultrasound in Medicine and Biology, 33(1), (2007).
[49] Y. Xu, L. V. Wang, G. Ambartsoumian *et al.*, "Reconstructions in limited-view thermoacoustic tomography," Medical physics, 31(4), 724-733 (2004).
[50] S. W. Huang, J. F. Eary, C. Jia *et al.*, "Differential-absorption photoacoustic imaging," Optics Letters, 34(16), 2393-2395 (2009).
[51] J. M. Vanderkooi, and D. F. Wilson, "A new method for measuring oxygen concentration in biological systems," Advances in experimental medicine and biology, 200, (1986).
[52] M. M. shenoi, N. B. Shah, R. J. Griffin *et al.*, "Nanoparticle preconditioning for enhanced thermal therapies in cancer," Nanomedicine, 6(3), (2011).
[53] J. S. Horoszewicz, S. S. Leong, E. Kawinski *et al.*, "LNCaP model of human prostatic carcinoma," Cancer Res, 43(4), 1809-18 (1983).
[54] C. A. Pettaway, S. Pathak, G. Greene *et al.*, "Selection of highly metastatic variants of different human prostatic carcinomas using orthotopic implantation in nude mice," Clinical Cancer Research, 2(9), (1996).
[55] C. Kim, T. N. Erpelding, L. Jankovic *et al.*, "Deeply penetrating in vivo photoacoustic imaging using a clinical ultrasound array system," Biomedical optics express, 1(1), 278-284 (2010).
[56] S. A. Ermilov, T. Khamapirad, A. Conjusteau *et al.*, "Laser optoacoustic imaging system for detection of breast cancer," Journal of Biomedical Optics, 14(2), 024007 (2009).
[57] R. G. Kolkman, P. J. Brands, W. Steenbergen *et al.*, "Real-time in vivo photoacoustic and ultrasound imaging," Journal of Biomedical Optics, 13(5), 050510 (2008).
[58] D. Abele, "The radical life-giver," Nature, 420(6911), 27-27 (2002).
[59] M. Hockel, and P. Vaupel, "Tumor hypoxia: Definitions and current clinical, biologic, and molecular aspects," Journal of the National Cancer Institute, 93(4), 266-276 (2001).
[60] U. K. Franzeck, P. Talke, E. F. Bernstein *et al.*, "Transcutaneous PO2 measurements in health and peripheral arterial occlusive disease," Surgery, 91(2), 156-63 (1982).

[61] J. Ditzel, "Oxygen transport impairment in diabetes," Diabetes, 25(2 SUPPL), 832-8 (1976).

[62] D. Laurent, C. Bolene-Williams, F. L. Williams *et al.*, "Effects of heart rate on coronary flow and cardiac oxygen consumption," Amer Jour Physiol, 185((2)), 355-364 (1956).

[63] C. J. Schofield, and P. J. Ratcliffe, "Oxygen sensing by HIF hydroxylases," Nature Reviews Molecular Cell Biology, 5(5), 343-354 (2004).

[64] H. W. Hopf, T. K. Hunt, J. M. West *et al.*, "Wound tissue oxygen tension predicts the risk of wound infection in surgical patients," Archives of Surgery, 132(9), 997-1004 (1997).

[65] N. Chang, W. H. Goodson, F. Gottrup *et al.*, "DIRECT MEASUREMENT OF WOUND AND TISSUE OXYGEN-TENSION IN POSTOPERATIVE-PATIENTS," Annals of Surgery, 197(4), 470-478 (1983).

[66] A. Villringer, J. Planck, C. Hock *et al.*, "NEAR-INFRARED SPECTROSCOPY (NIRS) - A NEW TOOL TO STUDY HEMODYNAMIC-CHANGES DURING ACTIVATION OF BRAIN-FUNCTION IN HUMAN ADULTS," Neuroscience Letters, 154(1-2), 101-104 (1993).

[67] P. V. Prasad, R. R. Edelman, and F. H. Epstein, "Noninvasive evaluation of intrarenal oxygenation with BOLD MRI," Circulation, 94(12), 3271-3275 (1996).

[68] T. M. Suszynski, E. S. Avgoustiniatos, S. A. Stein *et al.*, "Assessment of Tissue-Engineered Islet Graft Viability by Fluorine Magnetic Resonance Spectroscopy," Transplantation Proceedings, 43(9), 3221-3225 (2011).

[69] R. C. Urtasun, M. B. Parliament, A. J. McEwan *et al.*, "Measurement of hypoxia in human tumours by non-invasive spect imaging of iodoazomycin arabinoside," The British journal of cancer. Supplement, 27, S209-12 (1996).

[70] D. Wu, L. Huang, M. S. Jiang *et al.*, "Contrast Agents for Photoacoustic and Thermoacoustic Imaging: A Review," International Journal of Molecular Sciences, 15(12), 23616-23639 (2014).

[71] P. L. Olive, J. P. Banath, and C. Aquino-Parsons, "Measuring hypoxia in solid tumours - Is there a gold standard?," Acta Oncologica, 40(8), 917-923 (2001).

[72] J. R. Griffiths, and S. P. Robinson, "The OxyLite: a fibre-optic oxygen sensor," British Journal of Radiology, 72(859), 627-630 (1999).

[73] I. A. Barbazetto, J. H. Liang, S. Chang *et al.*, "Oxygen tension in the rabbit lens and vitreous before and after vitrectomy," Experimental Eye Research, 78(5), 917-924 (2004).

[74] W. Zhong, P. Urayama, and M. A. Mycek, "Imaging fluorescence lifetime modulation of a ruthenium-based dye in living cells: the potential for oxygen sensing," Journal of Physics D-Applied Physics, 36(14), 1689-1695 (2003).

[75] R. D. Shonat, D. F. Wilson, C. E. Riva *et al.*, "OXYGEN DISTRIBUTION IN THE RETINAL AND CHOROIDAL VESSELS OF THE CAT AS MEASURED BY A NEW PHOSPHORESCENCE IMAGING METHOD," Applied Optics, 31(19), 3711-3718 (1992).

[76] U. Noeth, P. Groehn, A. Jork *et al.*, “19F-MRI in vivo determination of the partial oxygen pressure in perfluorocarbon-loaded alginate capsules implanted into the peritoneal cavity and different tissues,” Magnetic Resonance in Medicine, 42(6), 1039-1047 (1999).

[77] O. Optics, [Oxygen Probes & Fibers], (2015).

[78] [http://www.pyro-science.com/overview-fiber-optic-oxygen-sensors.html].

[79] [http://oceanoptics.com/product-category/oxygen-probes-and-fibers/].

[80] M. H. Xu, and L. H. V. Wang, “Photoacoustic imaging in biomedicine,” Review of Scientific Instruments, 77(4), (2006).

[81] Q. Shao, E. Morgounova, C. Jiang *et al.*, “In vivo photoacoustic lifetime imaging of tumor hypoxia in small animals,” Journal of Biomedical Optics, 18(7), 076019-076019 (2013).

[82] Q. Shao, E. Morgounova, and S. Ashkenazi, "Direct tissue oxygen monitoring by in vivo photoacoustic lifetime imaging (PALI)." 8943, 89430F-89430F-6.

[83] Q. Shao, E. Morgounova, J.-H. Choi *et al.*, "Mapping tissue oxygen in vivo by photoacoustic lifetime imaging." 85811S-85811S-7.

[84] J. Laufer, C. Elwell, D. Delpy *et al.*, “In vitro measurements of absolute blood oxygen saturation using pulsed near-infrared photoacoustic spectroscopy: accuracy and resolution,” Physics in Medicine and Biology, 50(18), 4409-4428 (2005).

[85] J. Yao, K. I. Maslov, Y. Zhang *et al.*, “Label-free oxygen-metabolic photoacoustic microscopy in vivo,” Journal of Biomedical Optics, 16(7), (2011).

[86] H. F. Zhang, K. Maslov, M. Sivaramakrishnan *et al.*, “Imaging of hemoglobin oxygen saturation variations in single vessels in vivo using photoacoustic microscopy,” Applied Physics Letters, 90(5), (2007).

[87] D. Carnell, N. Taylor, R. Smith *et al.*, "Evaluation of prostate gland hypoxia with quantified BOLD MRI: updated results from a correlated histological study."

[88] A. Padhani, M. Ah-See, N. Taylor *et al.*, "An investigation of histological and DC-MRI correlates of intrinsic susceptibility contrast relaxivity (R2*) in human breast cancer."

[89] G. Atkin, N. Taylor, F. Daley *et al.*, “Dynamic contrast-enhanced magnetic resonance imaging is a poor measure of rectal cancer angiogenesis,” British journal of surgery, 93(8), 992-1000 (2006).

[90] J. M. Vanderkooi, and D. F. Wilson, [A new method for measuring oxygen concentration in biological systems] Springer, (1986).

[91] D. A. Dunn, V. H. Lin, and I. E. Kochevar, “THE ROLE OF GROUND-STATE COMPLEXATION IN THE ELECTRON-TRANSFER QUENCHING OF METHYLENE-BLUE FLUORESCENCE BY PURINE NUCLEOTIDES,” Photochemistry and Photobiology, 53(1), 47-56 (1991).

[92] R. Kiesslich, J. Fritsch, M. Holtmann *et al.*, “Methylene blue-aided chromoendoscopy for the detection of intraepithelial neoplasia and colon cancer in ulcerative colitis,” Gastroenterology, 124(4), 880-888 (2003).

[93] J. P. Tardivo, A. Del Giglio, C. S. de Oliveira *et al.*, "Methylene blue in photodynamic therapy: from basic mechanisms to clinical applications," Photodiagnosis and Photodynamic Therapy, 2(3), 175-191 (2005).
[94] P. National Toxicology, "Toxicology and carcinogenesis studies of methylene blue trihydrate (Cas No. 7220-79-3) in F344/N rats and B6C3F1 mice (gavage studies)," National Toxicology Program technical report series(540), 1-224 (2008).
[95] P. Burgholzer, G. J. Matt, M. Haltmeier *et al.*, "Exact and approximative imaging methods for photoacoustic tomography using an arbitrary detection surface," Physical Review E, 75(4), (2007).
[96] I. B. Tan, H. Oppelaar, M. C. Ruevekamp *et al.*, "The importance of in situ light dosimetry for photodynamic therapy of oral cavity tumors," Head & neck, 21(5), 434-441 (1999).
[97] P. Baas, L. Murrer, F. Zoetmulder *et al.*, "Photodynamic therapy as adjuvant therapy in surgically treated pleural malignancies," British journal of cancer, 76(6), 819 (1997).
[98] H. Schouwink, H. Oppelaar, M. Ruevekamp *et al.*, "Oxygen depletion during and after mTHPC-mediated photodynamic therapy in RIF1 and H-MESO1 tumors," (2009).
[99] B. Tromberg, A. Orenstein, S. Kimel *et al.*, "In vivo tumor oxygen tension measurements for the evaluation of the efficiency of photodynamic therapy," Photochemistry and photobiology, 52(2), 375-385 (1990).
[100] T. M. Busch, "Local physiological changes during photodynamic therapy," Lasers in surgery and medicine, 38(5), 494-499 (2006).
[101] P. Vaupel, K. Schlenger, C. Knoop *et al.*, "OXYGENATION OF HUMAN TUMORS - EVALUATION OF TISSUE OXYGEN DISTRIBUTION IN BREAST CANCERS BY COMPUTERIZED O2 TENSION MEASUREMENTS," Cancer Research, 51(12), 3316-3322 (1991).
[102] G. Helmlinger, F. Yuan, M. Dellian *et al.*, "Interstitial pH and pO2 gradients in solid tumors in vivo: high-resolution measurements reveal a lack of correlation," Nature medicine, 3(2), 177-182 (1997).
[103] M. Dewhirst, E. Ong, G. Rosner *et al.*, "Arteriolar oxygenation in tumour and subcutaneous arterioles: effects of inspired air oxygen content," The British journal of cancer. Supplement, 27, S241 (1996).
[104] B. M. Fenton, E. K. Rofstad, F. L. Degner *et al.*, "Cryospectrophotometric determination of tumor intravascular oxyhemoglobin saturations: dependence on vascular geometry and tumor growth," Journal of the National Cancer Institute, 80(20), 1612-1619 (1988).
[105] M. W. Dewhirst, E. T. Ong, B. Klitzman *et al.*, "Perivascular oxygen tensions in a transplantable mammary tumor growing in a dorsal flap window chamber," Radiation research, 130(2), 171-182 (1992).

[106] B. M. Fenton, and D. W. Siemann, [Investigations of perfusion-limited hypoxia and oxygenation in the KHT sarcoma] Springer, (1994).
[107] B. M. Fenton, and B. A. Way, "Vascular morphometry of KHT and RIF-1 murine sarcomas," Radiotherapy and Oncology, 28(1), 57-62 (1993).
[108] S.-M. Eschmann, F. Paulsen, M. Reimold *et al.*, "Prognostic impact of hypoxia imaging with 18F-misonidazole PET in non-small cell lung cancer and head and neck cancer before radiotherapy," Journal of Nuclear Medicine, 46(2), 253-260 (2005).
[109] C. F. Albiach, A. C. Moreno, M. R. Cordón *et al.*, "Contribution of hypoxia-measuring molecular imaging techniques to radiotherapy planning and treatment," Clinical and Translational Oncology, 12(1), 22-26 (2010).
[110] C. M. Doll, M. Milosevic, M. Pintilie *et al.*, "Estimating hypoxic status in human tumors: a simulation using Eppendorf oxygen probe data in cervical cancer patients," International Journal of Radiation Oncology* Biology* Physics, 55(5), 1239-1246 (2003).
[111] J. Williams, J. Stamp, R. Devonshire *et al.*, "Methylene blue and the photodynamic therapy of superficial bladder cancer," Journal of Photochemistry and Photobiology B: Biology, 4(2), 229-232 (1989).
[112] K. König, V. Bockhorn, W. Dietel *et al.*, "Photochemotherapy of animal tumors with the photosensitizer methylene blue using a krypton laser," Journal of cancer research and clinical oncology, 113(3), 301-303 (1987).
[113] K. Orth, G. Beck, F. Genze *et al.*, "Methylene blue mediated photodynamic therapy in experimental colorectal tumors in mice," Journal of Photochemistry and Photobiology B-Biology, 57(2-3), (2000).
[114] L. V. Wang, and S. Hu, "Photoacoustic Tomography: In Vivo Imaging from Organelles to Organs," Science, 335(6075), 1458-1462 (2012).
[115] C. L. Bayer, G. P. Luke, and S. Y. Emelianov, "Photoacoustic Imaging for Medical Diagnostics," Acoustics today, 8(4), 15-23 (2012).
[116] Y. Zhang, H. Hong, and W. Cai, "Photoacoustic imaging," Cold Spring Harb Protoc, 2011(9), (2011).
[117] A. H. Green, J. R. Norris, J. Wang *et al.*, "In vitro testing of a protease-sensitive contrast agent for optoacoustic imaging," Journal of Biomedical Optics, 15(2), 8 (2010).
[118] J. Levi, S. R. Kothapalli, T. J. Ma *et al.*, "Design, Synthesis, and Imaging of an Activatable Photoacoustic Probe," Journal of the American Chemical Society, 132(32), 11264-11269 (2010).
[119] P. C. Li, C. R. C. Wang, D. B. Shieh *et al.*, "In vivo Photoacoustic Molecular Imaging with Simultaneous Multiple Selective Targeting Using Antibody-Conjugated Gold Nanorods," Optics Express, 16(23), 18605-18615 (2008).
[120] S. Tyagi, and F. R. Kramer, "Molecular beacons: Probes that fluoresce upon hybridization," Nature Biotechnology, 14(3), 303-308 (1996).

[121] C. R. Drake, D. C. Miller, and E. F. Jones, "Activatable Optical Probes for the Detection of Enzymes," Current Organic Synthesis, 8(4), 498-520 (2011).
[122] D. Razansky, N. J. Harlaar, J. L. Hillebrands *et al.*, "Multispectral Optoacoustic Tomography of Matrix Metalloproteinase Activity in Vulnerable Human Carotid Plaques," Molecular Imaging and Biology, 14(3), 277-285 (2012).
[123] A. Dragulescu-Andrasi, S. R. Kothapalli, G. A. Tikhomirov *et al.*, "Activatable Oligomerizable Imaging Agents for Photoacoustic Imaging of Furin-Like Activity in Living Subjects," Journal of the American Chemical Society, 135(30), 11015-11022 (2013).
[124] J. Levi, S. R. Kothapalli, S. Bohndiek *et al.*, "Molecular Photoacoustic Imaging of Follicular Thyroid Carcinoma," Clinical Cancer Research, 19(6), 1494-1502 (2013).
[125] B. T. Cox, J. G. Laufer, and P. C. Beard, "The challenges for quantitative photoacoustic imaging," Proceedings of SPIE-The International Society for Optical Engineering. 7177(2009).
[126] C. H. Tung, "Fluorescent peptide probes for in vivo diagnostic imaging," Biopolymers, 76(5), 391-403 (2004).
[127] V. Ntziachristos, C.-H. Tung, C. Bremer *et al.*, "Fluorescence molecular tomography resolves protease activity in vivo," Nat Med, 8(7), 757-761 (2002).
[128] M. Heijblom, D. Piras, W. Xia *et al.*, "Visualizing breast cancer using the Twente photoacoustic mammoscope: What do we learn from twelve new patient measurements?," Optics Express, 20(11), 11582-11597 (2012).
[129] A. Garcia-Uribe, J. Zou, M. Duvic *et al.*, "In Vivo Diagnosis of Melanoma and Nonmelanoma Skin Cancer Using Oblique Incidence Diffuse Reflectance Spectrometry," Cancer Research, 72(11), 2738-2745 (2012).
[130] J. I. Clifton, and J. B. Leikin, "Methylene Blue," American Journal of Therapeutics, 10(4), 289-291 (2003).
[131] A. R. Disanto, and J. G. Wagner, "Pharmacokinetics of highly ionized drugs II: Methylene blue—absorption, metabolism, and excretion in man and dog after oral administration," Journal of Pharmaceutical Sciences, 61(7), 1086-1090 (1972).
[132] C. Peter, D. Hongwan, A. Kupfer *et al.*, "Pharmacokinetics and organ distribution of intravenous and oral methylene blue," European Journal of Clinical Pharmacology, 56(3), 247-250 (2000).
[133] R. W. Redmond, and J. N. Gamlin, "A compilation of singlet oxygen yields from biologically relevant molecules," Photochemistry and Photobiology, 70(4), 391-475 (1999).
[134] O. Yazdani, M. Irandoust, J. B. Ghasemi *et al.*, "Thermodynamic study of the dimerization equilibrium of methylene blue, methylene green and thiazole orange at various surfactant concentrations and different ionic strengths and in mixed solvents by spectral titration and chemometric analysis," Dyes and Pigments, 92(3), 1031-1041 (2012).

[135] K. Patil, R. Pawar, and P. Talap, "Self-aggregation of Methylene Blue in aqueous medium and aqueous solutions of Bu4NBr and urea," Physical Chemistry Chemical Physics, 2(19), 4313-4317 (2000).
[136] C. Gialeli, A. D. Theocharis, and N. K. Karamanos, "Roles of matrix metalloproteinases in cancer progression and their pharmacological targeting," Febs Journal, 278(1), 16-27 (2011).
[137] M. Stearns, and M. E. Stearns, "Evidence for increased activated metalloproteinase 2 (MMP-2a) expression associated with human prostate cancer progression," Oncology Research, 8(2), 69-75 (1996).
[138] D. Trudel, Y. Fradet, F. Meyer *et al.*, "Significance of MMP-2 expression in prostate cancer: An immunohistochemical study," Cancer Research, 63(23), 8511-8515 (2003).
[139] E. I. Deryugina, and J. P. Quigley, "Matrix metalloproteinases and tumor metastasis," Cancer and Metastasis Reviews, 25(1), 9-34 (2006).
[140] L. J. McCawley, and L. M. Matrisian, "Matrix metalloproteinases: multifunctional contributors to tumor progression," Molecular Medicine Today, 6(4), 149-156 (2000).
[141] T. Jiang, E. S. Olson, Q. T. Nguyen *et al.*, "Tumor imaging by means of proteolytic activation of cell-penetrating peptides," Proceedings of the National Academy of Sciences of the United States of America, 101(51), 17867-17872 (2004).
[142] B. K. Kay, M. P. Williamson, and P. Sudol, "The importance of being proline: the interaction of proline-rich motifs in signaling proteins with their cognate domains," Faseb Journal, 14(2), 231-241 (2000).
[143] J. Zhang, Y. L. Ma, S. S. Taylor *et al.*, "Genetically encoded reporters of protein kinase A activity reveal impact of substrate tethering," Proceedings of the National Academy of Sciences of the United States of America, 98(26), 14997-15002 (2001).
[144] S. B. Liu, J. Zhang, and Y. K. Xiang, "FRET-based direct detection of dynamic protein kinase A activity on the sarcoplasmic reticulum in cardiomyocytes," Biochemical and Biophysical Research Communications, 404(2), 581-586 (2011).
[145] V. V. Didenko, "DNA probes using fluorescence resonance energy transfer (FRET): Designs and applications," Biotechniques, 31(5), 1106-+ (2001).
[146] R. Weissleder, C. H. Tung, U. Mahmood *et al.*, "In vivo imaging of tumors with protease-activated near-infrared fluorescent probes," Nature Biotechnology, 17(4), 375-378 (1999).
[147] J. H. Ryu, A. Lee, J. H. Na *et al.*, "Optimization of matrix metalloproteinase fluorogenic probes for osteoarthritis imaging," Amino Acids, 41(5), 1113-1122 (2011).